Supporting Information:

Iminobispyrazole Photoswitches: Two Pyrazole Rings Can Be Better Than One

Jiarong Wu,[a,b] Clara Li,[a] Lasse Kreimendahl[a] and Jake L. Greenfield[a,b]*

[a] *Institut für Organische Chemie, Universität Würzburg, 97074 Würzburg, Germany*

[b] *Center for Nanosystems Chemistry (CNC), Universität Würzburg, 97074 Würzburg, Germany*

* Corresponding Author: Jake.Greenfield@uni-wuerzburg.de

Table of Contents

1. Materials and Methods

All reagents and solvents were purchased from commercial suppliers and used without further purification, unless specified. Solvents were dried with a commercial solvent purification system PS-M6-6/7-En from Inert Technologies. All synthesised photoswitches were stored under N_2, kept dark and dried under high-vacuum for at least 24 h prior to use.

UV/Vis Absorption. Spectra were recorded on a Jasco V-770 spectrophotometer, equipped with a Peltier cooling system (PAC-743R), or a diode array setup as detailed below in Section 1.2.1. Standard 10 mm pathlength quartz glass cuvettes (Fluorescence Cuvettes) from Hellma were used and a stirring bead was added. Measurements were run at 293.15 K, unless otherwise stated. Solutions for the UV/vis measurements were made using spectroscopy grade dry degassed solvents. A background measurement containing only the solvent used (or blank substrate for solid-state measurements) was recorded before measuring samples. This background was subtracted from the sample data using Origin Software.

High-Resolution Mass Spectrometry (HR-MS). Electrospray ionisation (ESI) HR-MS spectrograms were recorded on a Bruker Daltonics microTOF focus instrument with a resolution of 18.000 FWHM. Samples were prepared in MeCN with 1% formic acid and the instrument was run in positive mode.

NMR Spectroscopy. NMR spectra were recorded at 298 K using a Bruker Avance HD III 400 MHz spectrometer automatically tuned and matched to the correct operating frequencies. The ^{13}C NMR spectra are broad-band proton decoupled. TopSpin 4.2 and MestReNova 14.3.2 were used to apply phase and baseline corrections. ^{1}H and ^{13}C NMR spectra were referenced to the residual solvent peak. Signals are reported in terms of chemical shift (ppm) and coupling constants (Hz). Abbreviations for multiplicity are as follows: s, singlet; d, doublet; t, triplet; m, multiplet; br, broad; hept, heptet.

Quantum Yield of Photoswitching. The photon flux from the 340, 365, 385, 405 nm LEDs listed in Section 4.4 are determined in our previous work.[1] The $\boldsymbol{\Phi}_{ZE}$ and $\boldsymbol{\Phi}_{EZ}$ photoisomerization for the aryl imine photoswitches were determined using previously reported literature procedure and the calculation was performed using their provided software.[2] Collimated light was used when determining the photon flux, $\boldsymbol{\Phi}_{ZE}$, and $\boldsymbol{\Phi}_{EZ}$.

1.2 Diode Array Setup

The diode array setup schematically shown in Figure S1 was employed for Photostationary State (PSS), thermal half-life and quantum yield measurements.[1] The setup consists of an Ocean Insight DH-2000-FHS-DUV-TTL light source (190-2500 nm), connected to a Quantum Northwest QPod sample holder by 25 cm long premium fibre optics (Ocean Insight QP400-025-SR-BX). The temperature of the QPod sample holder was controlled using a Quantum Northwest TC 125 temperature controller, which also controlled the stirring. An Ocean Insight Flame-S-XR1-ES diode array spectrometer was used to measure the absorbance spectrum of the sample. Pin-hole slits were employed as shown in the schematic along with an optical filter at the light source to reduce the probe light intensity (Thermo Oriel 50550).

LEDs of various wavelengths (see Table S1 below) were employed to induce photoisomerization. These LEDs were fitted with adjustable collimation adapters supplied by ThorLabs (either a SM1U with an LA4052-UV Fused Silica Plano Convex Lens with an anti-reflective coating 245-400 nm or a SM1U25-A with an anti-reflective coating 350-700 nm, depending on the wavelength of the LED used). The LEDs were operated at a constant current mode controlled by a ThorLabs DC2200 LED driver.

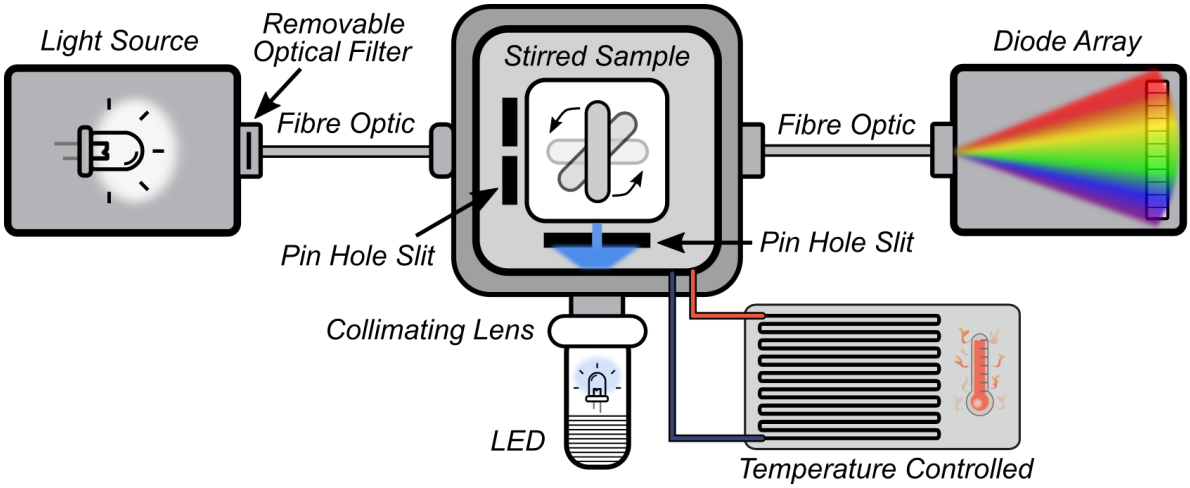

Figure S1. Schematic representation of the diode array setup up to measure the UV/vis absorption spectra and to perform photoswitching studies.

Table S1. Table displaying the models of ThorLabs mounted LEDs used in this study along with the nominal emission wavelength, the wavelength in which emission appears brightest to the human eye, and the bandwidth (full width at half maximum, FWHM).

LED model number (ThorLabs)	Wavelength (nm)	Bandwidth/FWHM (nm)
M340L5	340	10
M365L3	365	9
M385L3	385	11
M405L4	405	13

2. X-ray Crystallography

The collection of crystallographic data of the aryl imine photoswitches was obtained by using a Bruker D8 Quest diffractometer with a Photon II CMOS detector and Cu Kα radiation (λ = 1.54178 Å). A solution of the structure was performed with direct methods, refinement with the SHELX software package and expanding using Fourier techniques.[3] Nonhydrogen atoms were refined anisotropically while hydrogen atoms were positioned onto idealized positions and included in calculations of structure factors. CCDC 2370061 contains the supplementary crystallographic data for this paper. These data can be obtained free of charge from The Cambridge Crystallographic Data Centre via www.ccdc.cam.ac.uk/data_request/cif.

Table S2. X-ray structure characteristics for IBP *E*-**4,4**.

		E-**4,4**
	Empirical Formula	$C_9H_{11}N_5$
	$M_{empirical}$ (g mol^{-1})	189.23
	Wavelength (Å)	1.54178
	T (K)	100
Crystal Description	Colour	Colourless
	Habit	Needle
	Crystal System	Monoclinic
	Space Group	P2(1)/c
Unit Cell Dimensions	a (Å)	12.5417(18)
	b (Å)	8.2315(10)
	c (Å)	9.3787(8)
	α (°)	90
	β (°)	101.952(7)
	γ (°)	90
	Volume (Å^3)	947.2(2)
	Z	4
	$\rho_{alc.}$ (g cm^{-3})	1.327
	F(000)	400
	Range of θ (°)	3.602 72.323
	Goodness of Fit	1.071
	CCDC	2370061

3. Synthesis and Characterisation

Synthesis of (*E*)-*N*,1-bis(1-methyl-1*H*-pyrazol-3-yl)methanimine, (3,3)

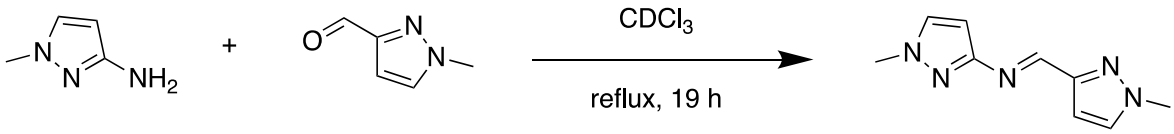

3,3

Isolated yield: 37%

In oven-dried glassware charged with 3 Å molecular sieves, 3-amino-1-methylpyrazole (131.1 mg, 1.4 mmol, 1.5 eq) and 3-carbaldehyde-1-methylpyrazole (100.0 mg, 0.9 mmol, 1.0 eq) were dissolved in $CDCl_3$ (2.0 mL) under an N_2 atmosphere. The mixture was heated under reflux for 19 hours, and the reaction completion was determined by TLC. The solvent was removed *in vacuo* and the resulting solid was purified using flash column chromatography with an eluent of cyclohexane:ethyl acetate from 80:20 to 0:100 with 1% (volume) triethylamine to afford product *E*-**3,3** as a white crystalline solid.

Yield: NMR Yield: quantitative. Isolated Yield: 64.2 mg (0.3 mmol, 37%).

m.p.: 92-97 °C.

^{1}H NMR (400 MHz, MeCN-d_3, 298 K): $\delta = 8.73$ (s, 1H), 7.54 (d, $J = 2.4$ Hz, 1H), 7.43 (d, $J = 2.3$ Hz, 1H), 6.76 (d, $J = 2.3$ Hz, 1H), 6.29 (d, $J = 2.4$ Hz, 1H), 3.91 (s, 3H), 3.82 (s, 3H) ppm.

^{13}C NMR (101 MHz, MeCN-d_3, 298 K): $\delta = 153.8$, 132.7, 132.2, 132.7, 104.6, 96.8, 39.2, 39.0 ppm.

HR-MS: (ESI-TOF, positive, MeCN) for $[C_9H_{11}N_5+H]^+$: *m*/*z* calcd: 190.1087; found: 190.1091; 2.0 ppm error.

Synthesis of (*E*)-*N*-(1-methyl-1*H*-pyrazol-3-yl)-1-(1-methyl-1*H*-pyrazol-4-yl)methanimine, (3,4)

3,4

Isolated yield: 74%

In oven-dried glassware charged with 3 Å molecular sieves, 3-amino-1-methylpyrazole (131.1 mg, 1.4 mmol, 1.5 eq) and 4-carbaldehyde-1-methylpyrazole (100.0 mg, 0.9 mmol, 1.0 eq) were dissolved in $CDCl_3$ (2.0 mL) under an N_2 atmosphere. The mixture was heated under reflux for 19 hours, and the reaction completion was determined by TLC. The solvent was removed *in vacuo* and the resulting solid was purified using flash column chromatography with an eluent of cyclohexane:ethyl acetate from 80:20 to 0:100 with 1% (volume) triethylamine to afford product **3,4** as a colorless oil.

Yield: NMR Yield: quantitative. Isolated Yield: 126.3 mg (0.7 mmol, 74%).

^{1}H NMR: (400 MHz, MeCN-d_3, 298 K): δ 8.69 (s, 1H), 7.93 (s, 1H), 7.85 (s, 1H), 7.40 (d, $J = 2.3$, 1H), 6.17 (d, $J = 2.3$, 1H), 3.88 (s, 3H), 3.80 (s, 3H) ppm.

^{13}C NMR (101 MHz, MeCN-d_3, 298 K): $\delta =$ 160.1, 152.8, 139.6, 132.7, 132.5, 122.4, 97.2, 39.5, 39.3 ppm.

HR-MS: (ESI-TOF, positive, MeCN) for $[C_9H_{11}N_5+H]^+$: *m*/*z* calcd: 190.1087; found: 190.1092; 2.6 ppm error.

Synthesis of (*E*)-*N*-(1-methyl-1*H*-pyrazol-3-yl)-1-(1-methyl-1*H*-pyrazol-5-yl)methanimine, (3,5)

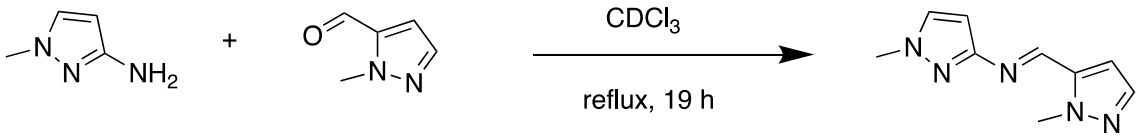

3,5

Isolated yield: 60%

In oven-dried glassware charged with 3 Å molecular sieves, 3-amino-1-methylpyrazole (131.1 mg, 1.4 mmol, 1.5 eq) and 5-carbaldehyde-1-methylpyrazole (100.0 mg, 0.9 mmol, 1.0 eq) were dissolved in $CDCl_3$ (2.0 mL) under an N_2 atmosphere. The mixture was heated under reflux for 19 hours, and the reaction completion was determined by TLC. The solvent was removed *in vacuo* and the resulting solid was purified using flash column chromatography with an eluent of cyclohexane:ethyl acetate from 80:20 to 0:100 with 1% (volume) triethylamine to afford product **3,5** as a colorless oil.

Yield: NMR Yield: quantitative. Isolated Yield: 103.2 mg (0.5 mmol, 60 %).

^{1}H NMR: (400 MHz, MeCN-d_3, 298 K): δ 8.81 (s, 1H), 7.46 (m, 2H), 6.74 (d, J = 2.0 Hz, 1H), 6.31 (d, J = 2.4 Hz, 1H), 4.15 (s, 3H), 3.83 (s, 3H) ppm.

^{13}C NMR (101 MHz, MeCN-d_3, 298 K): δ =159.2, 149.1, 139.7, 139.0, 132.9, 110.7, 97.7, 39.5, 39.3 ppm.

HR-MS: (ESI-TOF, positive, MeCN) for $[C_9H_{11}N_5+H]^+$: *m*/*z* calcd: 190.1087; found: 190.1093; 3.1 ppm error.

Synthesis of (*E*)-1-(1-methyl-1*H*-pyrazol-3-yl)-*N*-(1-methyl-1*H*-pyrazol-4-yl)methanimine, (4,3)

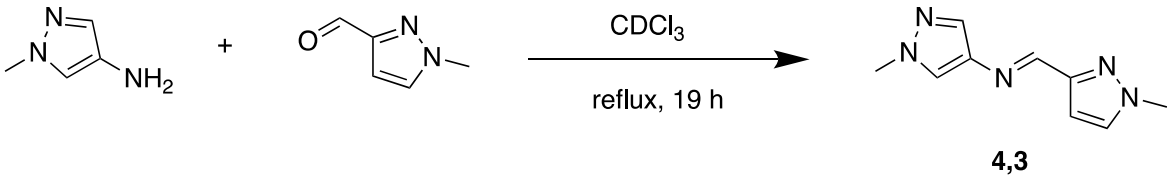

4,3

Isolated yield: 54%

In oven-dried glassware charged with 3 Å molecular sieves, 4-amino-1-methylpyrazole (131.1 mg, 1.4 mmol, 1.5 eq) and 3-carbaldehyde-1-methylpyrazole (100.0 mg, 0.9 mmol, 1.0 eq) were dissolved in $CDCl_3$ (2.0 mL) under an N_2 atmosphere. The mixture was heated under reflux for 19 hours, and the reaction completion was determined by TLC. The solvent was removed *in vacuo* and the resulting solid was purified using flash column chromatography with an eluent of cyclohexane:ethyl acetate from 80:20 to 0:100 with 1% (volume) triethylamine to afford product **4,3** as a white crystalline solid.

Yield: NMR Yield: quantitative. Isolated Yield: 93.2 mg (0.5 mmol, 54 %).

m.p.: 118 – 122 °C.

^{1}H-NMR: (400 MHz, MeCN-d_3, 298 K): δ 8.57 (s, 1H), 7.63 (s, 1H), 7.59 (s, 1H), 7.51 (d, J = 2.3 Hz, 1H), 6.67 (d, J = 2.3 Hz, 1H), 3.89 (s, 3H), 3.82 (s, 3H) ppm.

^{13}C NMR (101 MHz, MeCN-d_3, 298 K): δ =152.1, 151.6, 136.8, 132.9, 132.0, 125.0, 104.5, 39.7, 39.5 ppm.

HR-MS: (ESI-TOF, positive, MeCN) for $[C_9H_{11}N_5+H]^+$: *m*/*z* calcd: 190.1087; found: 190.1093; 3.3 ppm error.

Synthesis of (*E*)-*N*,1-bis(1-methyl-1*H*-pyrazol-4-yl)methanimine, (4,4)

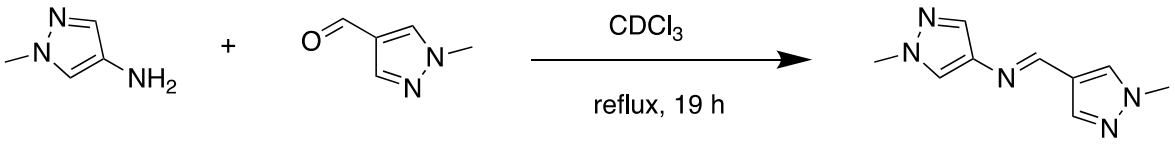

4,4

Isolated yield: 30%

In oven-dried glassware charged with 3 Å molecular sieves, 4-amino-1-methylpyrazole (131.1 mg, 1.4 mmol, 1.5 eq) and 4-carbaldehyde-1-methylpyrazole (100.0 mg, 0.9 mmol, 1.0 eq) were dissolved in $CDCl_3$ (2.0 mL) under an N_2 atmosphere. The mixture was heated under reflux for 19 hours, and the reaction completion was determined by TLC. The solvent was removed *in vacuo* and the resulting solid was purified using flash column chromatography with an eluent of cyclohexane:ethyl acetate from 80:20 to 0:100 with 1% (volume) triethylamine to afford product **4,4** as a pink crystalline solid.

Yield: NMR Yield: quantitative. Isolated Yield: 52.4 mg (0.3 mmol, 30%).

m.p.: 140 – 144 °C.

^{1}H NMR: (400 MHz, MeCN-d_3, 298 K): δ 8.49 (s, 1H), 7.85 (s, 1H), 7.78 (s, 1H), 7.54 (d, $J = 0.8$ Hz, 1H), 7.50 (d, $J = 0.8$ Hz, 1H), 3.87 (s, 3H), 3.81 (s, 3H) ppm.

^{13}C NMR (101 MHz, MeCN-d_3, 298 K): δ = 150.8, 139.1, 131.9, 131.6, 124.3, 39.5, 39.4 ppm.

HR-MS: (ESI-TOF, positive, MeCN) for $[C_9H_{11}N_5+H]^+$: *m*/*z* calcd: 190.1087; found: 190.1087; 0.3 ppm error.

Synthesis of (*E*)-*N*-(1-methyl-1*H*-pyrazol-4-yl)-1-(1-methyl-1*H*-pyrazol-5-yl)methanimine, (4,5)

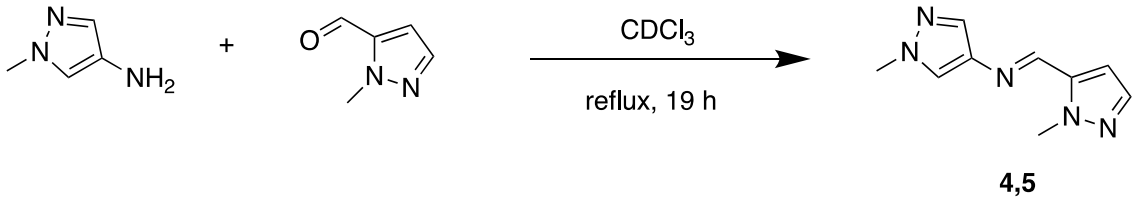

4,5

Isolated yield: 48%

In oven-dried glassware charged with 3 Å molecular sieves, 4-amino-1-methylpyrazole (131.1 mg, 1.4 mmol, 1.5 eq) and 5-carbaldehyde-1-methylpyrazole (100.0 mg, 0.9 mmol, 1.0 eq) were dissolved in $CDCl_3$ (2.0 mL) under an N_2 atmosphere. The mixture was heated under reflux for 19 hours, and the reaction completion was determined by TLC. The solvent was removed *in vacuo* and the resulting solid was purified using flash column chromatography with an eluent of cyclohexane:ethyl acetate from 80:20 to 0:100 with 1% (volume) triethylamine to afford product **4,5** as a beige solid.

Yield: NMR Yield: quantitative. Isolated Yield: 81.6 mg (0.4 mmol, 48%)

m.p.: 76-78 °C.

^{1}H NMR: (400 MHz, MeCN-d_3, 298 K): δ 8.62 (s, 1H), 7.66 (d, $J = 0.9$ Hz, 1H), 7.62 (d, $J = 0.9$ Hz, 1H), 7.44 (d, $J = 2.0$, 1H), 6.65 (s, $J = 2.0$ Hz, 1H), 4.11 (s, 3H), 3.84 (s, 3H) ppm.

^{13}C NMR (101 MHz, MeCN-d_3, 298 K): δ =147.0, 140.0, 139.0, 136.5, 131.9, 125.5, 109.4, 39.6, 39.0 ppm.

HR-MS: (ESI-TOF, positive, MeCN) for $[C_9H_{11}N_5+H]^+$: *m*/*z* calcd: 190.1087; found: 190.1093; 3.2 ppm error.

Synthesis of (*E*)-1-(1-methyl-1*H*-pyrazol-3-yl)-*N*-(1-methyl-1*H*-pyrazol-5-yl)methanimine, (5,3)

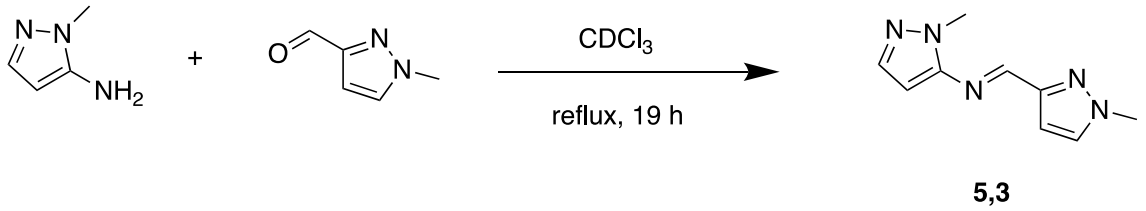

5,3

Isolated yield: 74%

In oven-dried glassware charged with 3 Å molecular sieves, 5-amino-1-methylpyrazole (131.1 mg, 1.4 mmol, 1.5 eq) and 3-carbaldehyde-1-methylpyrazole (100.0 mg, 0.9 mmol, 1.0 eq) were dissolved in $CDCl_3$ (2.0 mL) under an N_2 atmosphere. The mixture was heated under reflux for 19 hours, and the reaction completion was determined by TLC. The solvent was removed *in vacuo* and the resulting solid was purified using flash column chromatography with an eluent of ethyl acetate:methanol from 100:0 to 95:5 with 1% (volume) triethylamine to afford product **5,3** as a colorless oil.

Yield: NMR Yield: quantitative. Isolated Yield: 126.0 mg (0.6 mmol, 74%)

^{1}H NMR: (400 MHz, MeCN-d_3, 298 K): δ 8.63 (s, 1H), 7.55 (d, $J = 2.3$ Hz, 1H), 7.37 (d, $J = 2.1$ Hz, 1H), 6.83 (d, $J = 2.3$ Hz, 1H), 6.29 (d, $J = 2.1$ Hz, 1H), 3.91 (s, 3H), 3.85 (s, 3H) ppm.

^{13}C NMR (101 MHz, MeCN-d_3, 298 K): δ =154.8, 150.9, 150.6, 139.0, 133.3, 105.6, 92.5, 39.7, 35.1 ppm.

HR-MS: (ESI-TOF, positive, MeCN) for $[C_9H_{11}N_5+H]^+$: *m*/*z* calcd: 190.1087; found: 190.1090; 1.4 ppm error.

Synthesis of (*E*)-1-(1-methyl-1*H*-pyrazol-4-yl)-*N*-(1-methyl-1*H*-pyrazol-5-yl)methanimine, (5,4)

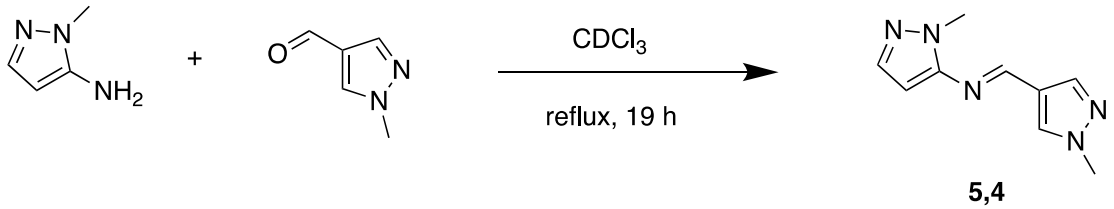

5,4

Isolated yield: 58%

In oven-dried glassware charged with 3 Å molecular sieves, 5-amino-1-methylpyrazole (131.1 mg, 1.4 mmol, 1.5 eq) and 4-carbaldehyde-1-methylpyrazole (100.0 mg, 0.9 mmol, 1.0 eq) were dissolved in $CDCl_3$ (2.0 mL) under an N_2 atmosphere. The mixture was heated under reflux for 19 hours, and the reaction completion was determined by TLC. The solvent was removed *in vacuo* and the resulting solid was purified using flash column chromatography with an eluent of cyclohexane:ethyl acetate of 1:1 with 1% (volume) triethylamine to afford product **5,4** as a colorless waxy solid.

Yield: NMR Yield: quantitative. Isolated Yield: 99.1 mg (0.5 mmol, 58%)

^{1}H NMR: (400 MHz, MeCN-d_3, 298 K): δ 8.58 (s, 1H), 7.99 (s, 1H), 7.91 (s, 1H), 7.34 (d, $J = 2.1$ Hz, 1H), 6.16 (d, $J = 2.1$ Hz, 1H), 3.90 (s, 3H), 3.82 (s, 3H) ppm.

^{13}C NMR (101 MHz, MeCN-d_3, 298 K): δ =153.8, 151.2, 140.0, 139.0, 133.3, 122.2, 91.9, 39.7, 35.0 ppm.

HR-MS: (ESI-TOF, positive, MeCN) for $[C_9H_{11}N_5+H]^+$: *m*/*z* calcd: 190.1087; found: 190.1096; 4.8 ppm error.

Synthesis of (*E*)-*N*,1-bis(1-methyl-1*H*-pyrazol-5-yl)methanimine, (5,5)

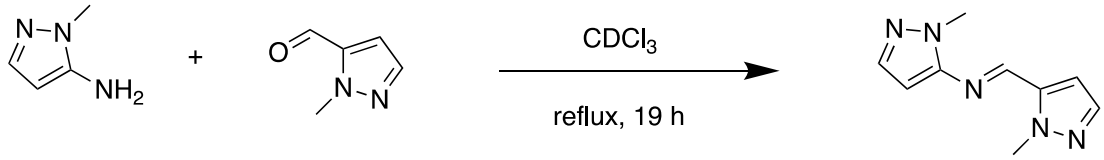

5,5

Isolated yield: 60%

In oven-dried glassware charged with 3 Å molecular sieves, 5-amino-1-methylpyrazole (131.1 mg, 1.4 mmol, 1.5 eq) and 5-carbaldehyde-1-methylpyrazole (100.0 mg, 0.9 mmol, 1.0 eq) were dissolved in $CDCl_3$ (2.0 mL) under an N_2 atmosphere. The mixture was heated under reflux for 19 hours, and the reaction completion was determined by TLC. The solvent was removed *in vacuo* and the resulting solid was purified using flash column chromatography with an eluent of cyclohexane:ethyl acetate from 80:20 to 0:100 with 1% (volume) triethylamine to afford product **5,5** as a white crystalline solid.

Yield: NMR Yield: quantitative. Isolated Yield: 103.2 mg (0.5 mmol, 60 %)

m.p.: 68-72 °C.

^{1}H NMR: (400 MHz, MeCN-d_3, 298 K): δ 8.66 (s, 1H), 7.49 (d, J = 2.0 Hz, 1H), 7.40 (d, J = 2.2 Hz, 1H), 6.80 (d, J = 2.1 Hz, 1H), 6.32 (d, J = 2.1 Hz, 1H), 4.19 (s, 3H), 3.87 (s, 3H) ppm.

^{13}C NMR (101 MHz, MeCN-d_3, 298 K): δ = 149.4, 139.2, 139.1, 111.8, 92.5, 39.9, 35.3 ppm.

HR-MS: (ESI-TOF, positive, MeCN) for $[C_9H_{11}N_5+H]^+$: m/z calcd: 190.1087; found: 190.1093; 3.0 ppm error.

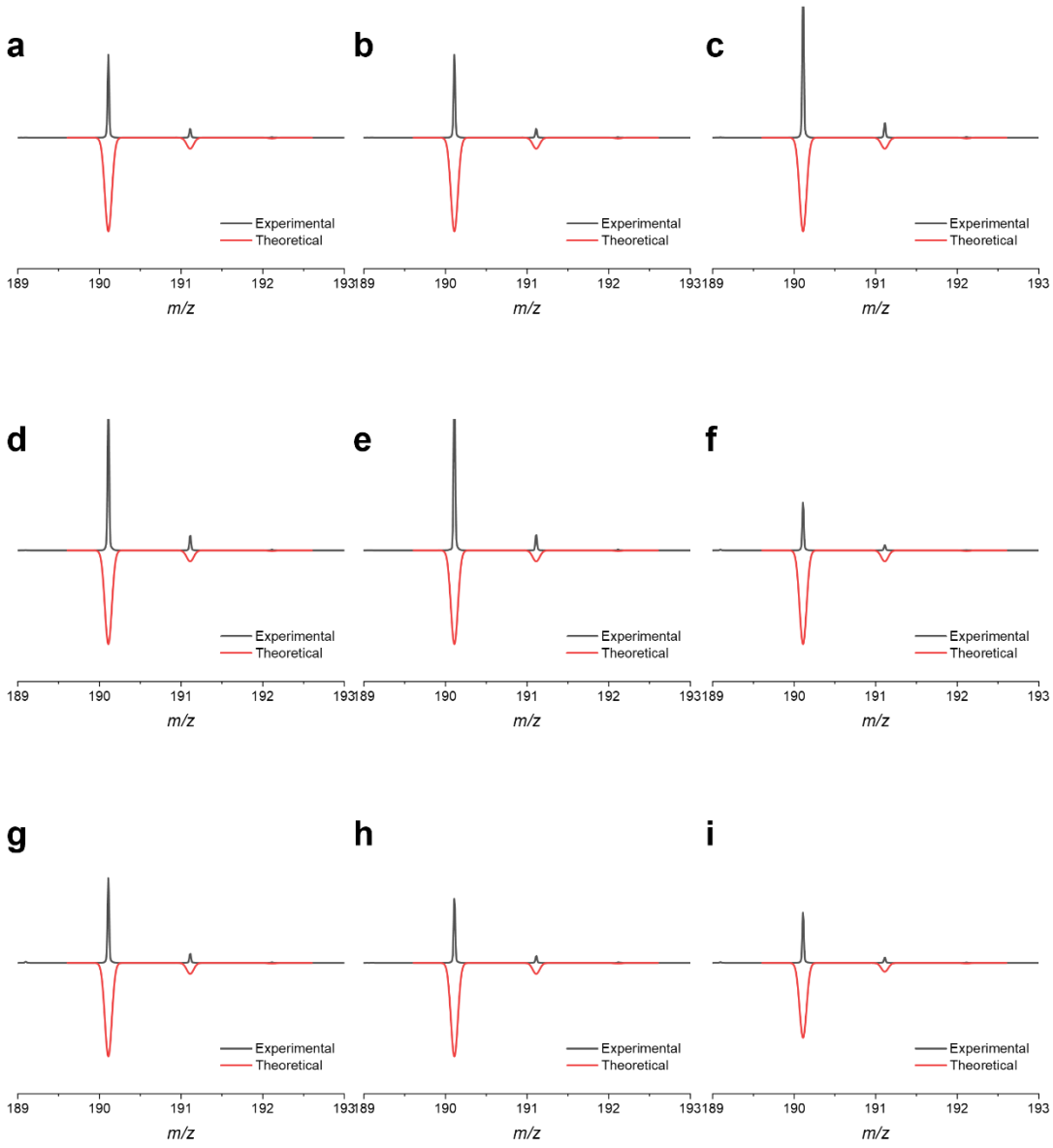

Figure S2. The HR-MS (ESI) peaks of the IBPs with a proton displayed in blue; (a) **3,3** at 190.1091, (b) **3,4** at 109.1092, (c) **3,5** at 190.1093, (d) **4,3** at 190.1094, (e) **4,4** at 190.1088, (f) **4,5** at 190.1093, (g) **5,3** at 190.1090, (h) **5,4** at 190.1096 and (i) **5,5** at 190.1093 *m/z*. The related theoretical isotope patterns are displayed in red and reflected on the x-axis.

4. Photoswitching Properties

Table S3. Overview of the photostationary state (PSS), thermal half-life and quantum yield (QY) of photoisomerism data for the various wavelengths of irradiation used. The PSS and QY values are obtained from UV/vis measurements performed in MeCN at 20°C.

	λ_{max} (nm)	$t_{1/2}$	%*Z* at PSS			QY (%)	
			340 nm	365 nm	385 nm	340 nm	365 nm
3,3	296	6.5 min	41%	11%	-	7 (1)	-
3,4	301	25.8 min	58%	15%	-	2 (0)	-
3,5	307	1.4 min	54%	28%	-	5 (0)	-
4,3	305	6.5 min	40%	7%	-	2 (0)	-
4,4	304	26.3 min	48%	7%	-	-	-
4,5	315	2.2 min	46%	21%	-	5 (1)	-
5,3[a]	315	50.4 s	–%[b]	–%[b]	-	-	-
5,4	316	3.4 min	76%	54%	18%	4 (9)	-
5,5[a]	324	17.0 s	–%[b]	–%[b]	-	2 (5)	3 (7)

[a] Note that the short $t_{1/2}$ values preclude the measurement of the %*Z* at the PSS under these conditions due to a significant amount of *Z*-to-*E* thermal reversion taking place during photoisomerism. [b] The PSS could not be determined at 20 °C.

4.1 Extinction Coefficient

The UV/vis spectra of all imines included in this work were measured using a Jasco V-770 UV/vis/NIR spectrophotometer at various concentrations. According to Beer-Lambert Law,[4] there exists a linear relationship between the absorbance and the concentration of the solution, which can be expressed as:

$$A = \epsilon l c$$

In this equation, "*A*" represents the absorbance in absorbance units (a.u.), "*l*" is the optical path length, which is typically the width of the cuvette used for the absorbance measurement (1 cm), and "*c*" is the molar concentration in moles per liter (M). From the absorption spectra (Figure S3-S11), the molar extinction coefficient (ε) at the specific wavelength (λ_{max}) can be determined by fitting a linear calibration curve of the absorbance versus concentration.

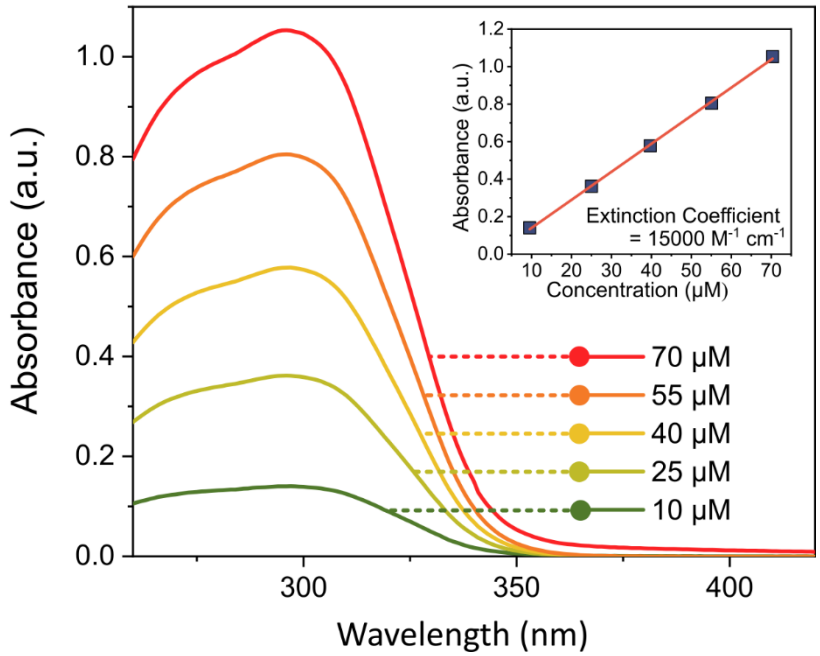

Figure S3. UV/vis absorption spectra of IBP **3,3** in MeCN at five different concentrations, measured at 20 °C. The top right corner shows the calibration curve, which was plotted at λ_{max} to determine the slope, which gives the extinction coefficient.

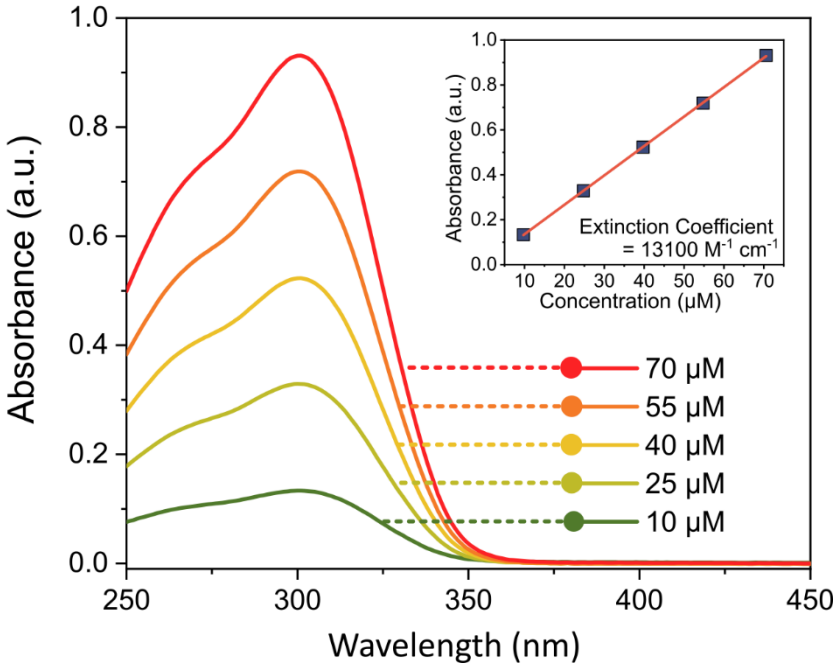

Figure S4. UV/vis absorption spectra of IBP **3,4** in MeCN at five different concentrations, measured at 20 °C. The top right corner shows the calibration curve, which was plotted at λ_{max} to determine the slope, which gives the extinction coefficient.

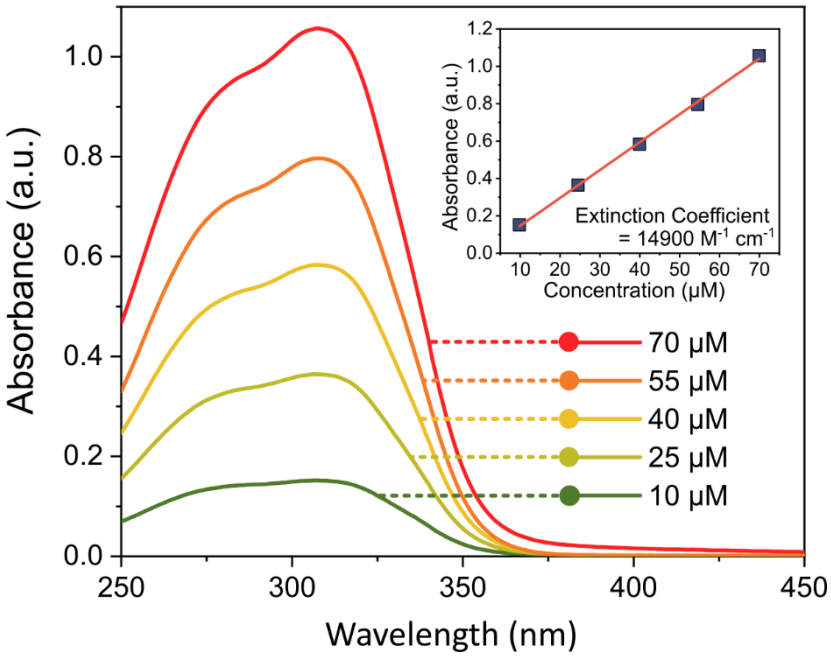

Figure S5. UV/vis absorption spectra of IBP **3,5** in MeCN at five different concentrations, measured at 20 °C. The top right corner shows the calibration curve, which was plotted at λ_{max} to determine the slope, which gives the extinction coefficient.

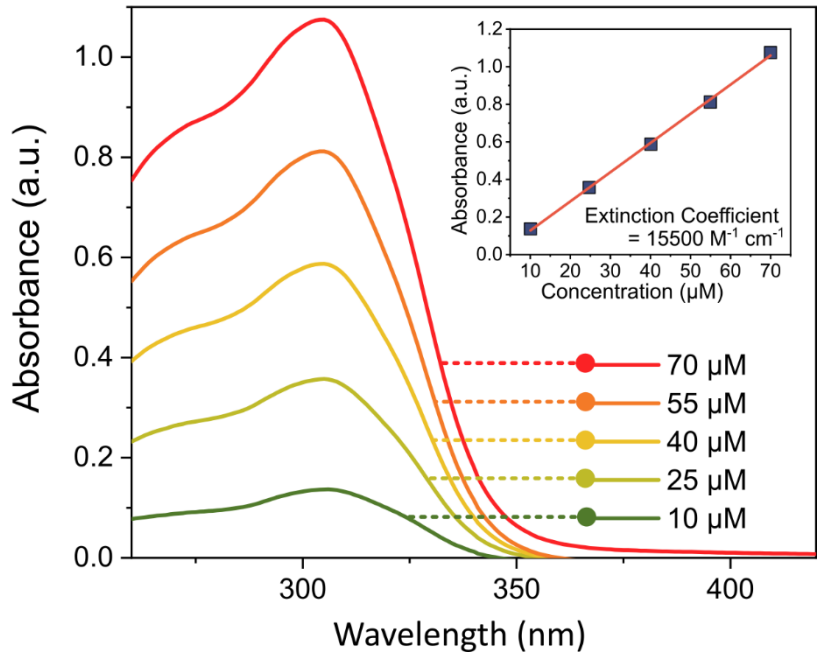

Figure S6. UV/vis absorption spectra of IBP **4,3** in MeCN at five different concentrations, measured at 20 °C. The top right corner shows the calibration curve, which was plotted at λ_{max} to determine the slope, which gives the extinction coefficient.

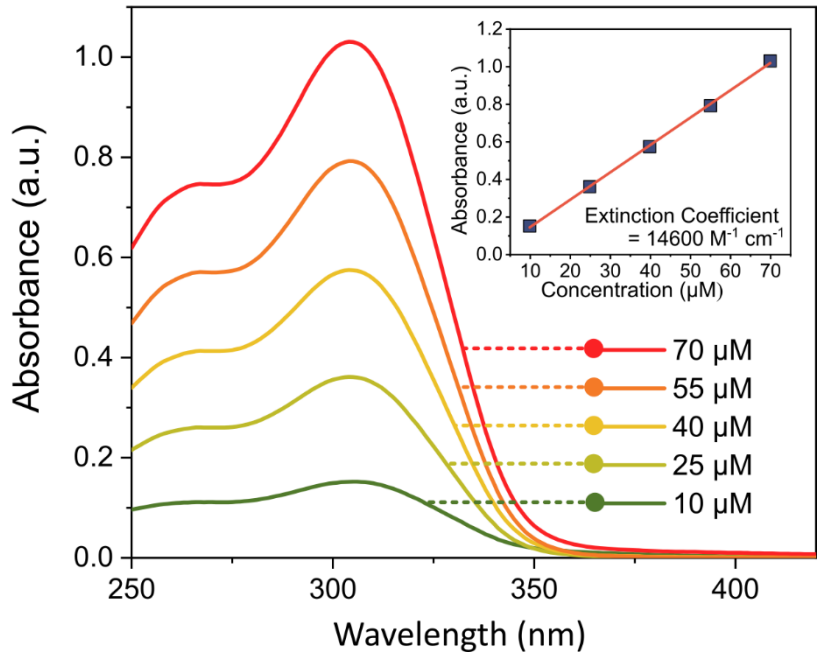

Figure S7. UV/vis absorption spectra of IBP **4,4** in MeCN at five different concentrations, measured at 20 °C. The top right corner shows the calibration curve, which was plotted at λ_{max} to determine the slope, which gives the extinction coefficient.

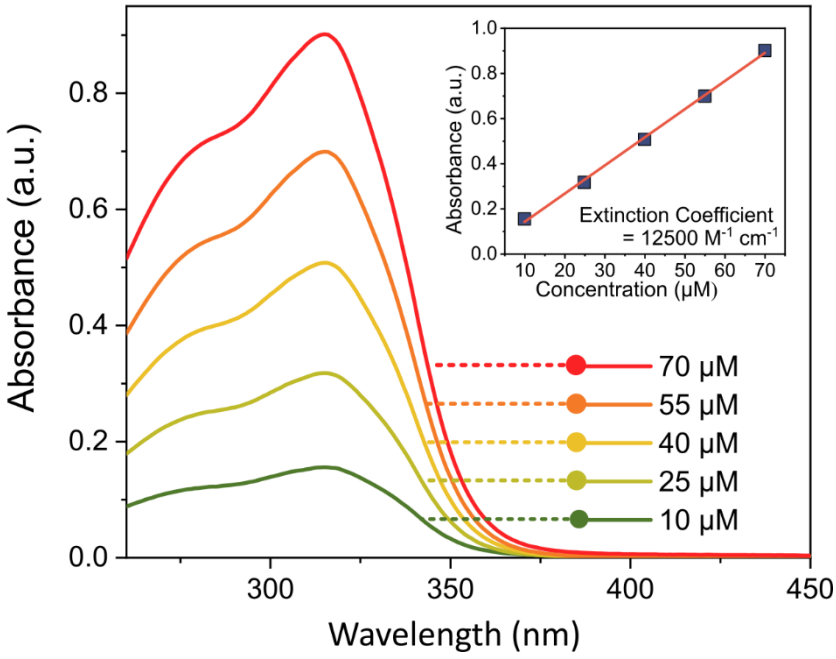

Figure S8. UV/vis absorption spectra of IBP **4,5** in MeCN at five different concentrations, measured at 20 °C. The top right corner shows the calibration curve, which was plotted at λ_{max} to determine the slope, which gives the extinction coefficient.

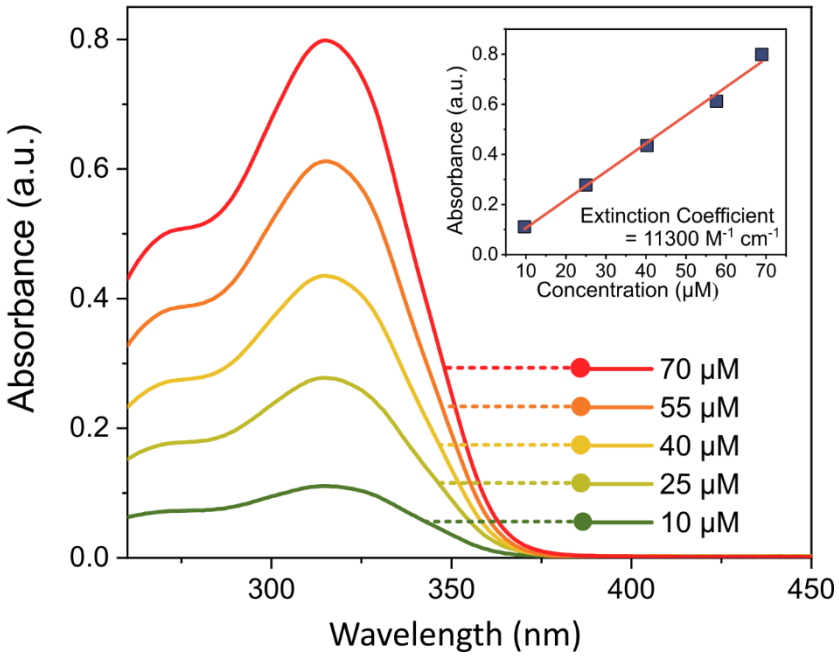

Figure S9. UV/vis absorption spectra of IBP **5,3** in MeCN at five different concentrations, measured at 20 °C. The top right corner shows the calibration curve, which was plotted at λ_{max} to determine the slope, which gives the extinction coefficient.

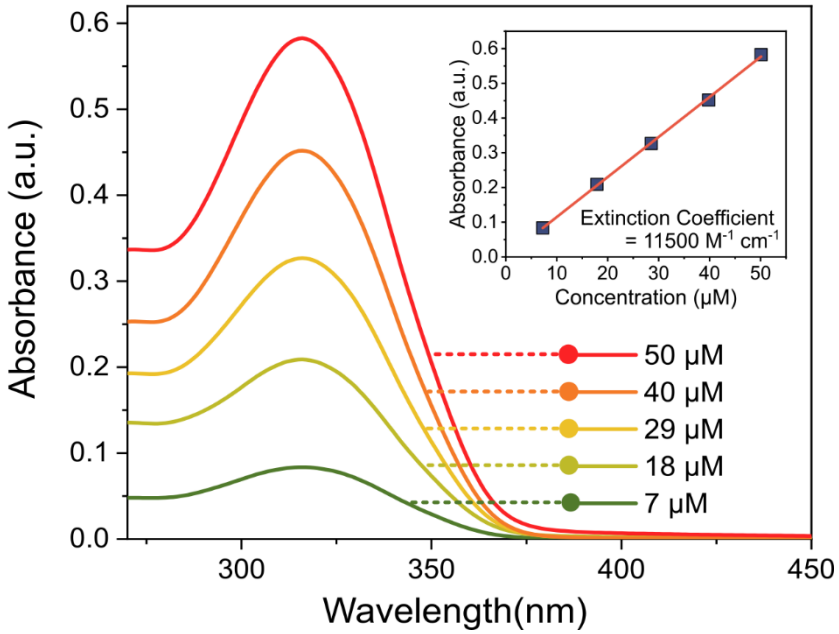

Figure S10. UV/vis absorption spectra of IBP **5,4** in MeCN at five different concentrations, measured at 20 °C. The top right corner shows the calibration curve, which was plotted at λ_{max} to determine the slope, which gives the extinction coefficient.

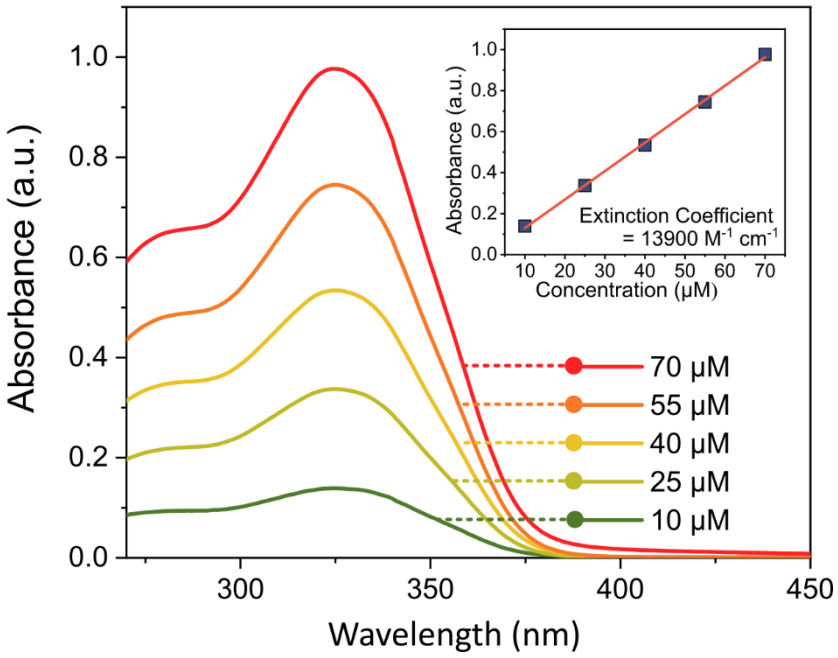

Figure S11. UV/vis absorption spectra of IBP **5,5** in MeCN at five different concentrations, measured at 20 °C. The top right corner shows the calibration curve, which was plotted at λ_{max} to determine the slope, which gives the extinction coefficient.

4.2 Thermodynamic Properties

The kinetics of all imine switches included in this work were investigated using the diode array setup (Section 1.2 of the Supporting Information). These measurements were conducted in the solution state using acetonitrile as the solvent, and a range of temperatures was employed for linear Eyring plots. The isomerization from *E*-isomers to *Z*-isomers was induced by irradiation with 365 nm LED light. Assuming first-order reactions, the rate constants (k) for the thermodynamic switching process from *Z*- to *E*-state were determined by fitting the absorbance changes over time to an exponential (Figures S12-S20), and the thermal half-lives ($t_{1/2}$) were calculated based on this rate constants.

Utilizing the linearized form of the Eyring equation presented below:[5]

$$ln\,\frac{k}{T} = \frac{-\Delta H^{\ddagger}}{R}\cdot\frac{1}{T} + ln\,\frac{k_B}{h} + \frac{\Delta S^{\ddagger}}{R}$$

The values for enthalpy of activation ($\Delta H^{\ddagger}$) and entropy of activation ($\Delta S^{\ddagger}$) in Table S4 can be determined from the kinetic data at different temperatures by linear fitting (Figure S12-S20). Gibbs energy of activation (listed in Table S4) can be calculated using the Gibbs function:

$$\Delta G^{\ddagger} = \Delta H^{\ddagger} - T\Delta S^{\ddagger}$$

Table S4. The summary of activation parameters including thermal half-life (at 20 °C), enthalpy of activation ($\Delta H^{\ddagger}$), entropy of activation ($\Delta S^{\ddagger}$), and Gibbs energy of activation ($\Delta G^{\ddagger}$) data of imines discussed in this work. In this table, the Gibbs energy of activation corresponds to a temperature of 295K.

	$t_{1/2}$	$\Delta H^{\ddagger}$ (kJ·mol^{-1})	$\Delta S^{\ddagger}$ (J·K^{-1}·mol^{-1})	$\Delta G^{\ddagger}$ (kJ·mol^{-1})
3,3	6.5 min	80.3	-23	87.3
3,4	25.8 min	85.9	-15.8	90.5
3,5	1.4 min	82.8	-2	83.4
4,3	6.5 min	77	-35	88
4,4	26.3 min	71.4	-63.3	90.1
4,5	2.2 min	80.8	-13	84.7
5,3	50.4 s	82.7	1.0	82.5
5,4	3.4 min	88.1	8.9	85.5
5,5	17.0 s	81.3	6.1	79.5

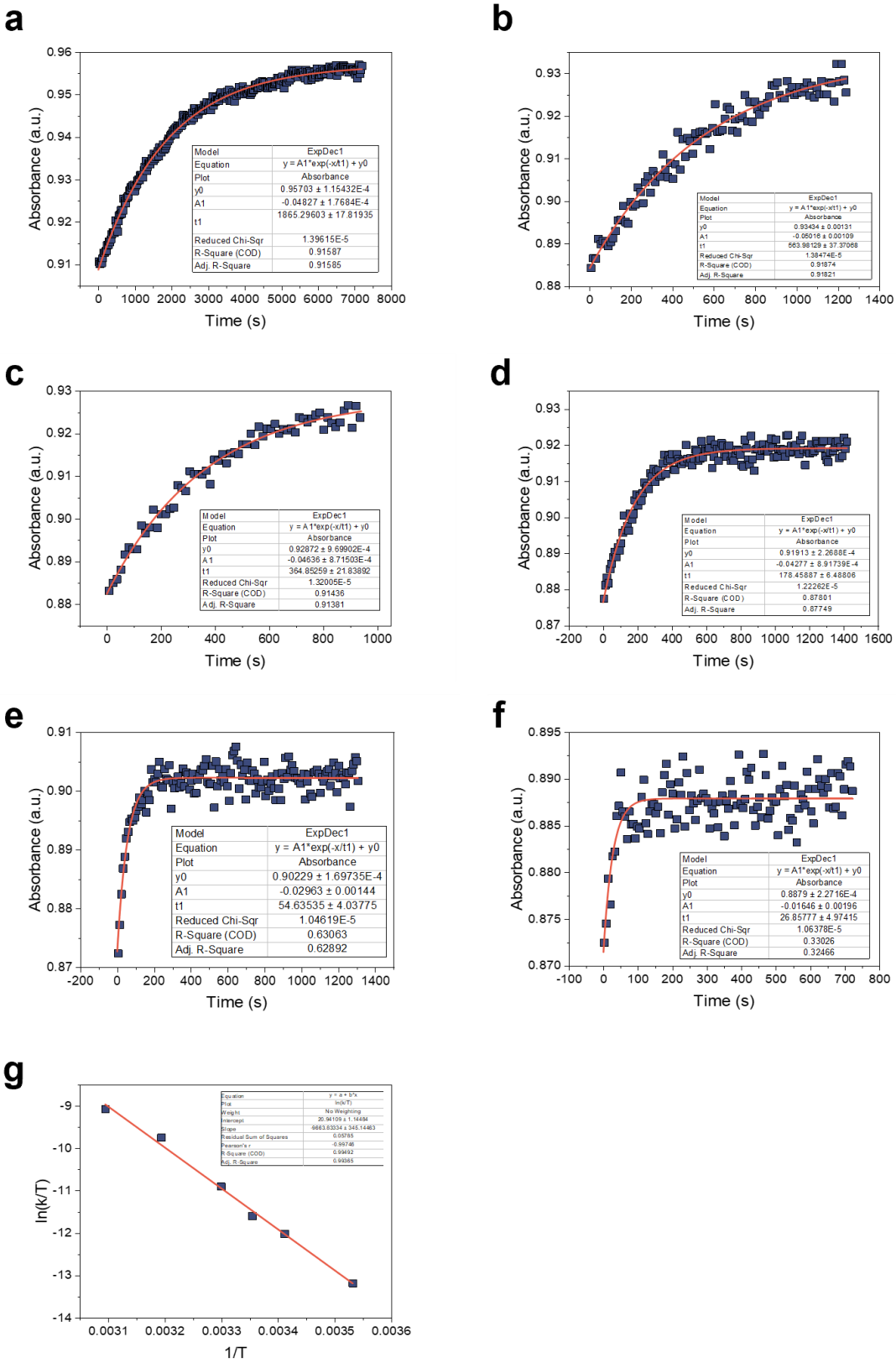

Figure S12. The change in absorbance of **3,3** at λ_{max} of the *E*-isomer over time at various temperatures: (a) 10 °C (b) 20 °C (c) 25 °C (d) 30 °C (e) 40 °C (f) 50 °C. (g) The Eyring plot generated by using the rate constants calculated at the different temperatures. The measurements were carried out in MeCN (70 μM).

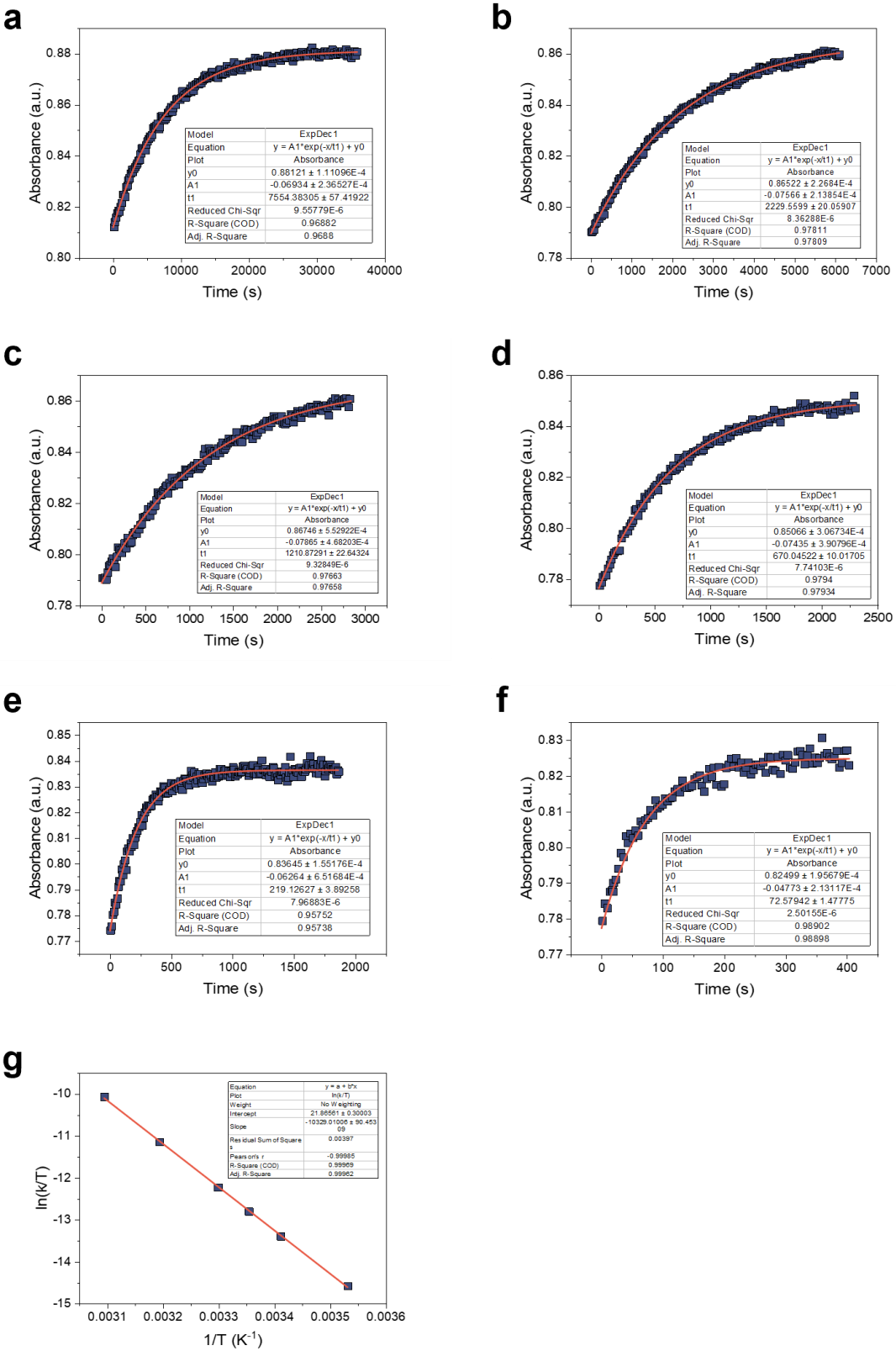

Figure S13. The increase in absorbance of **3,4** at λ_{max} of the *E*-isomer over time at various temperatures: (a) 10 °C (b) 20 °C (c) 25 °C (d) 30 °C (e) 40 °C (f) 50 °C. (g) The Eyring plot generated by using the rate constants calculated at the different temperatures. The measurements were carried out in MeCN (70 μM).

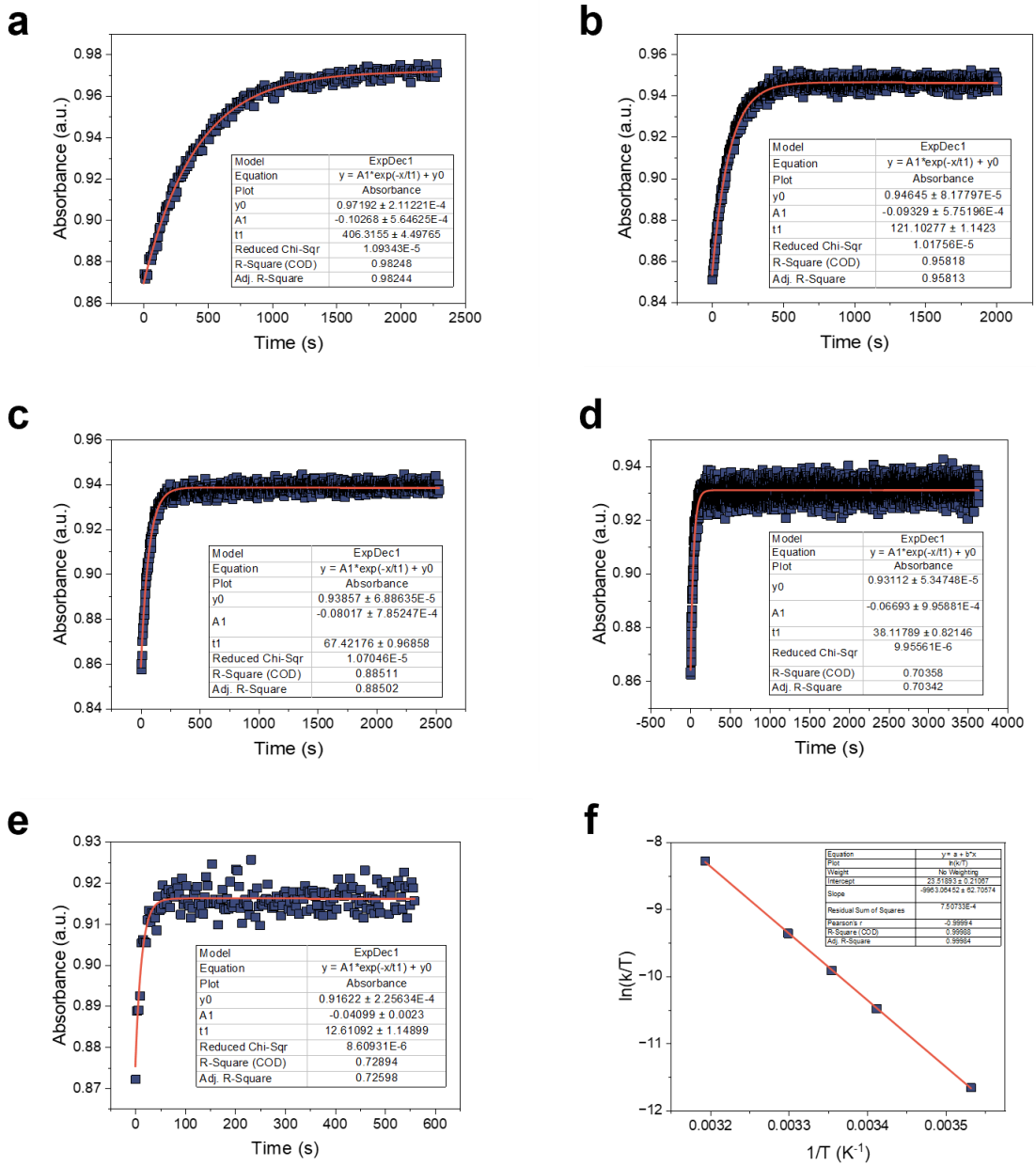

Figure S14. The increase in absorbance of **3,5** at λ_{max} of the *E*-isomer over time at various temperatures: (a) 10 °C (b) 20 °C (c) 25 °C (d) 30 °C (e) 40 °C. (f) The Eyring plot generated by using the rate constants calculated at the different temperatures. The measurements were carried out in MeCN (70 μM).

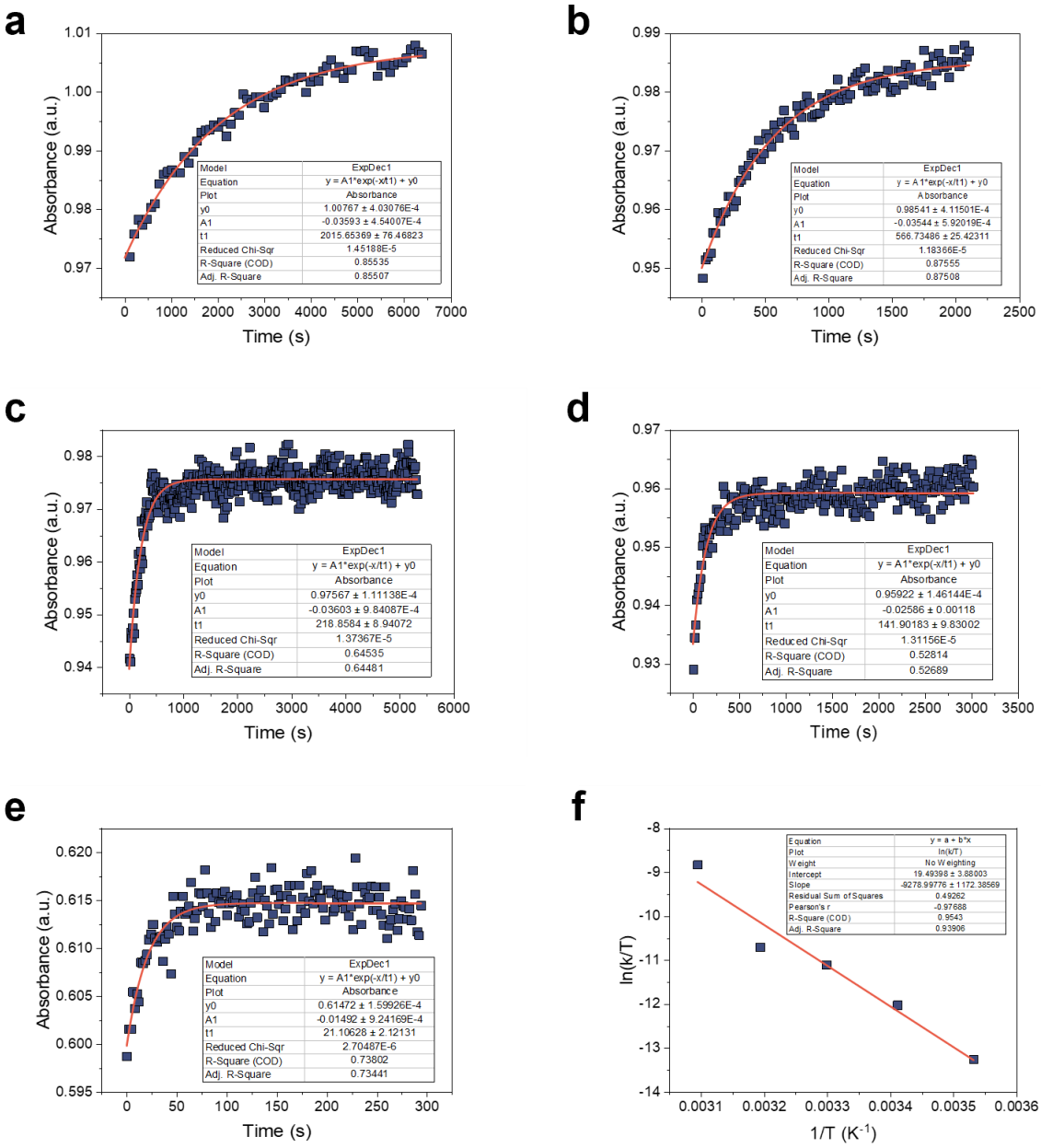

Figure S15. The increase in absorbance of **4,3** at λ_{max} of the *E*-isomer over time at various temperatures: (a) 10 °C (b) 20 °C (c) 30 °C (d) 40 °C (e) 50 °C. (f) The Eyring plot generated by using the rate constants calculated at the different temperatures. The measurements were carried out in MeCN (70 μM).

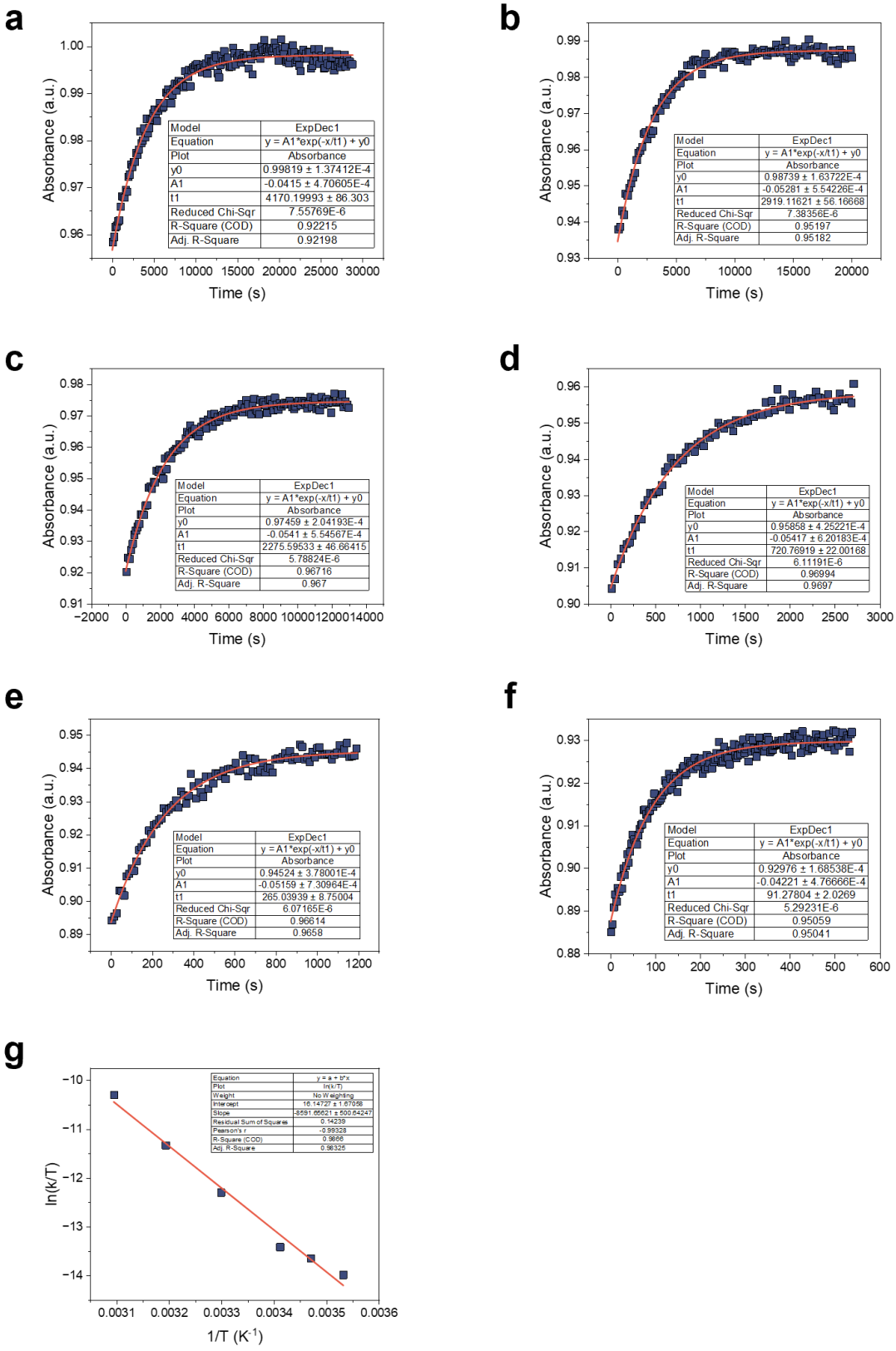

Figure S16. The increase in absorbance of **4,4** at λ_{max} of the *E*-isomer over time at various temperatures: (a) 10 °C (b) 20 °C (c) 25 °C (d) 30 °C (e) 40 °C (f) 50 °C. (g) The Eyring plot generated by using the rate constants calculated at the different temperatures. The measurements were carried out in MeCN (70 μM).

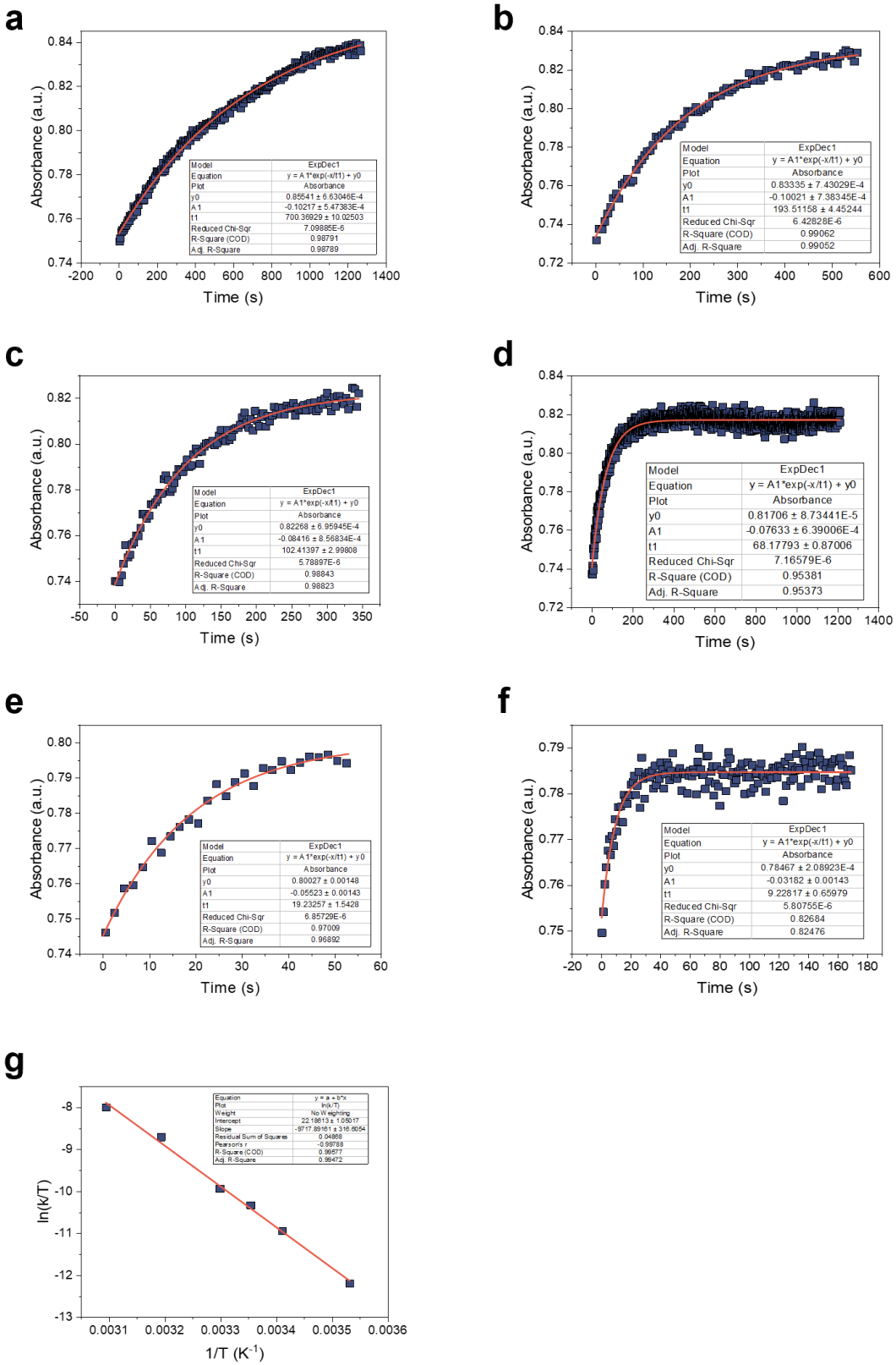

Figure S17. The increase in absorbance of **4,5** at λ_{max} of the *E*-isomer over time at various temperatures: (a) 10 °C (b) 20 °C (c) 25 °C (d) 30 °C (e) 40 °C (f) 50 °C. (g) The Eyring plot generated by using the rate constants calculated at the different temperatures. The measurements were carried out in MeCN (70 μM).

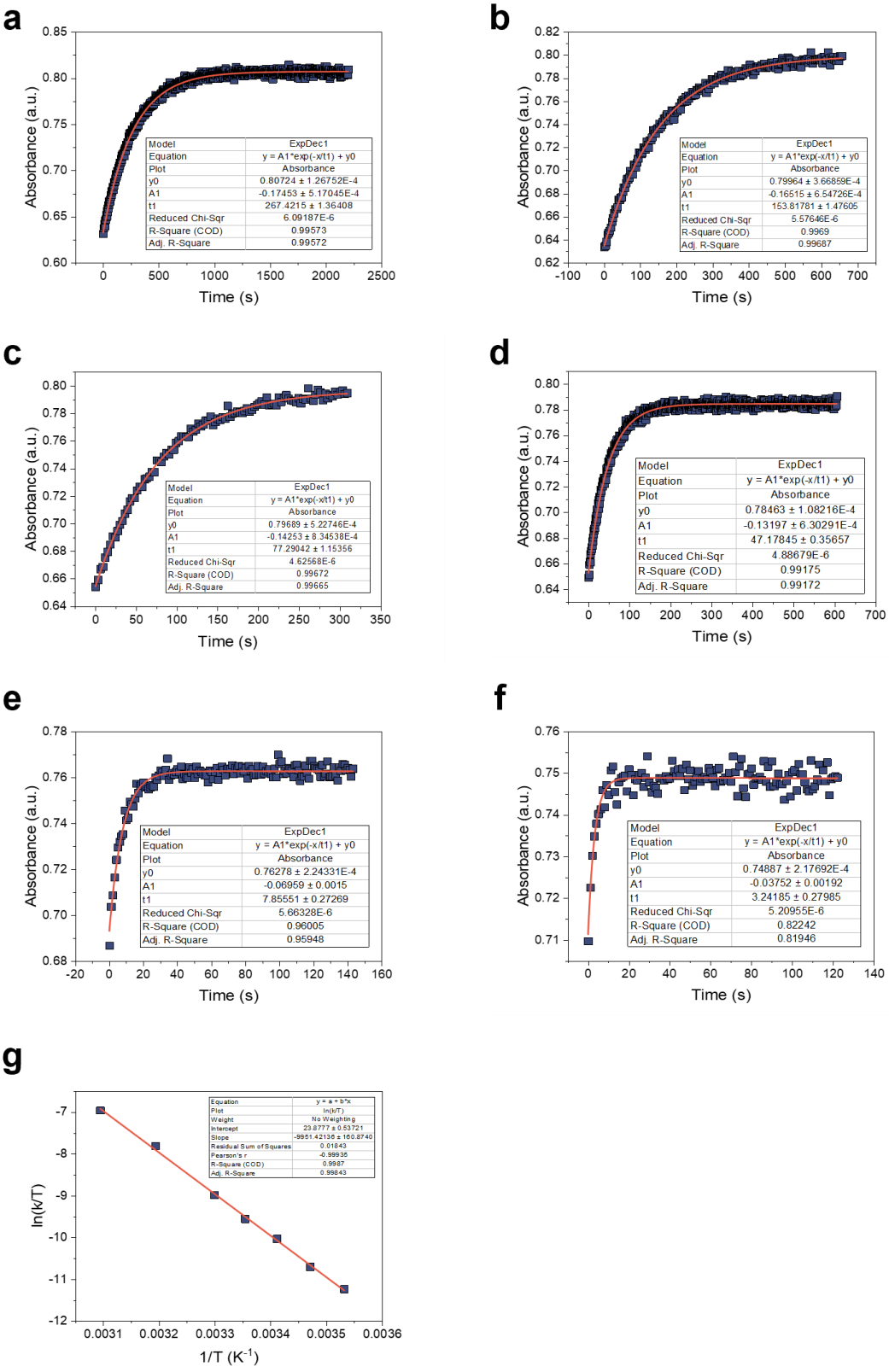

Figure S18. The increase in absorbance of **5,3** at λ_{max} of the *E*-isomer over time at various temperatures: (a) 10 °C (b) 20 °C (c) 25 °C (d) 30 °C (e) 40 °C (f) 50 °C. (g) The Eyring plot generated by using the rate constants calculated at the different temperatures. The measurements were carried out in MeCN (70 µM).

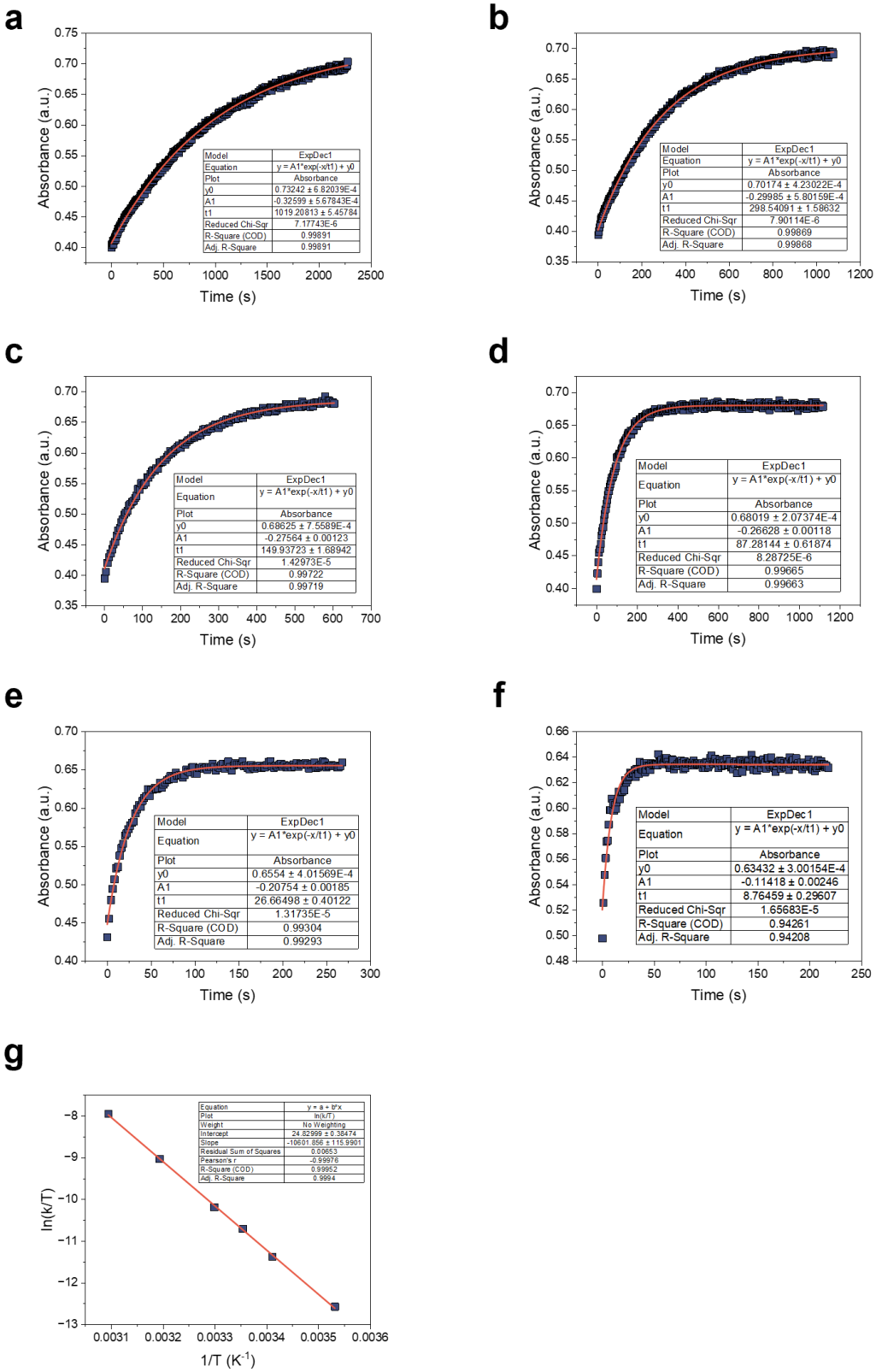

Figure 19. The change in absorbance of **5,4** at λ_{max} of the E-isomer over time at various temperatures: (a) 10 °C (b) 20 °C (c) 25 °C (d) 30 °C (e) 40 °C. (f) 50 °C. (g) The Eyring plot generated by using the rate constants calculated at the different temperatures. The measurements were carried out in MeCN (50 μM).

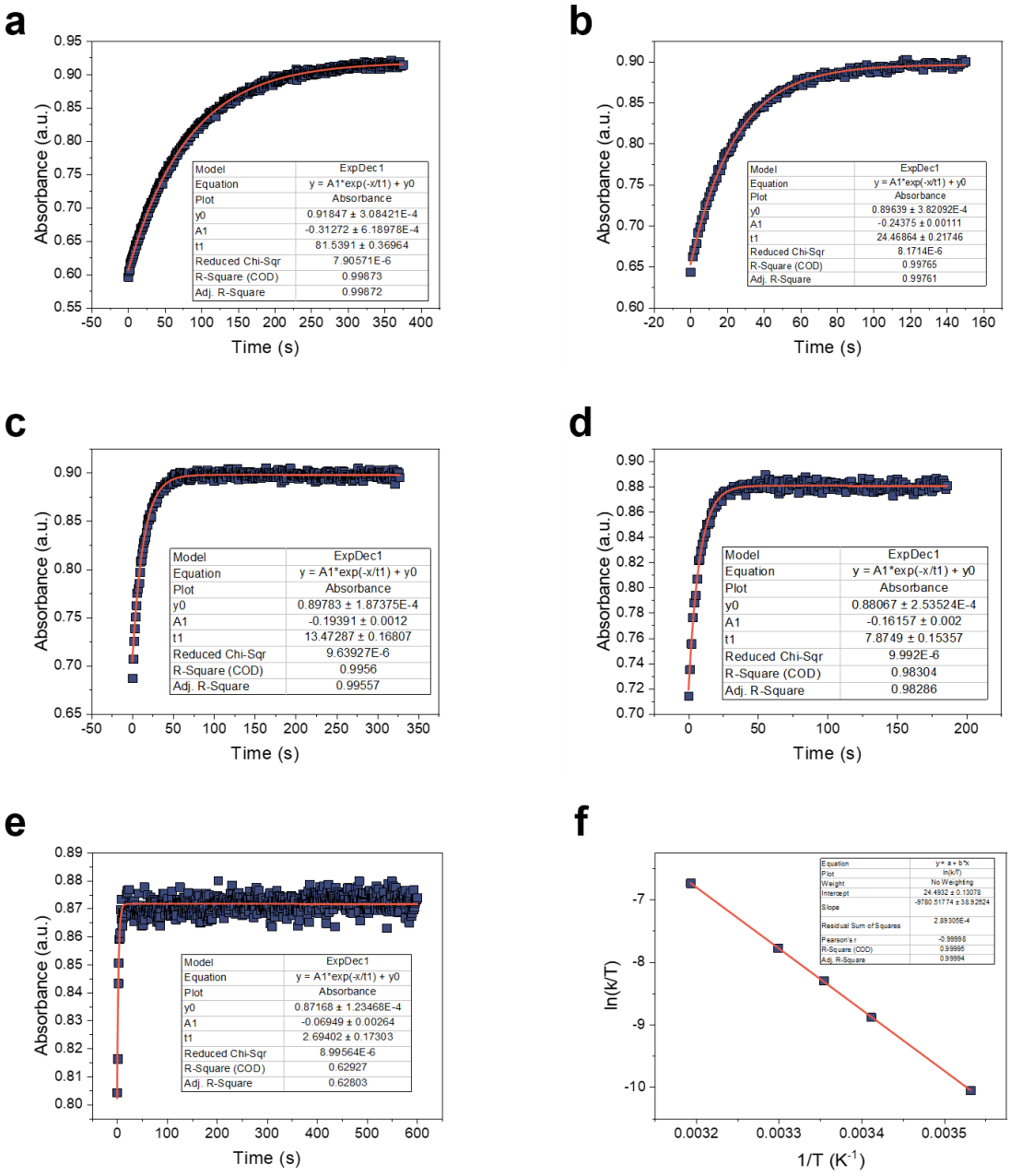

Figure S20. The change in absorbance of **5,5** at λ_{max} of the *E*-isomer over time at various temperatures: (a) 10°C (b) 20°C (c) 25°C (d) 30°C (e) 40 °C (f) The Eyring plot generated by using the rate constants calculated at the different temperatures. The measurements were carried out in MeCN (70 μM).

4.3 Photostationary State (PSS)

Irradiation for PSS measurements was conducted using the diode array setup (Section 1.2) with LED lights of 340 nm and 365 nm, as detailed in Table S1.

The proportions of the *Z*-isomers at the PSS reported in Table 1 and Table S3 were determined by UV/vis spectroscopy at 20 °C, using spectroscopy grade acetonitrile as the solvent. The calculations of PSS were performed according to Fischer's approach,[6] by analysing the absorption spectra of the pure *E*-isomer before irradiation and after photo-equilibration at two different wavelengths. From this, the UV/vis of the pure *Z*-isomer was predicted (see below).

The absorption spectra of *Z*-isomers can be estimated by the relationship between the dark spectra (Pure *E*), the PSS spectra and the PSS quantity, as presented below:

$$Estimated\ Pure\ Z = (Spectra\ of\ pure\ E) + \frac{(PSS\ spectra) - (Pure\ E\ spectra)}{(PSS\ quantity)}$$

It is important to note that our setup, shown schematically in Figure S1, facilitates the rapid acquisition of the UV/vis spectra: 50 ms integration time, average of 10 spectra, resulting in a spectrum being recorded every 0.5 s. The combination of the high intensity of irradiation, rapid spectral acquisition, and temperature control limits the amount of time between irradiation and spectral acquisition, providing a reliable measurement of the PSS at the given irradiation wavelength and temperature. Note that the underlying competing *Z*-to-*E* thermal relaxation process does influence the measured %*Z* isomer of the photoswitches with a short $t_{1/2}$, thus, we report the maximum measured %*Z* isomer for imines **5,3** and **5,5** since the PSS is not reached under these conditions.

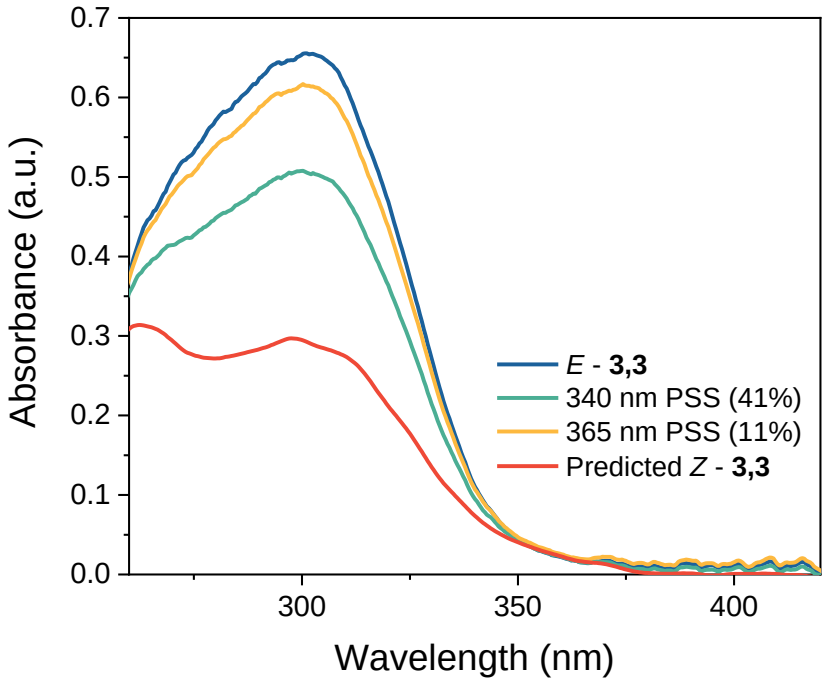

Figure S21. Absorbance spectra of the pure *E*-isomer and PSS at 340 and 365 nm and predicted absorbance spectra for the pure *Z*-isomer of IBP **3,3**. The measurements were carried out in MeCN (60 μM) at room temperature (20 °C).

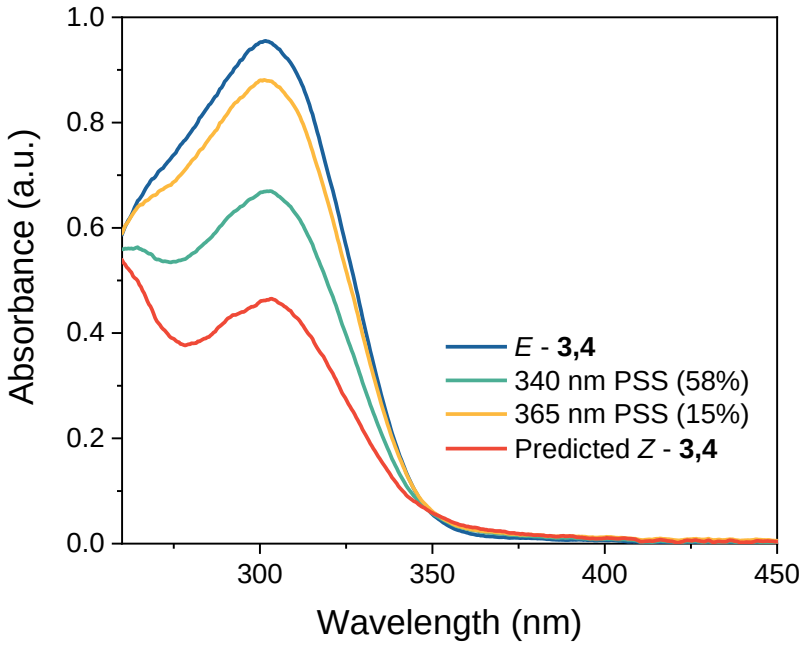

Figure S22. Absorbance spectra of the pure *E*-isomer and PSS at 340 and 365 nm and predicted absorbance spectra for the pure *Z*-isomer of IBP **3,4**. The measurements were carried out in MeCN (70 μM) at room temperature (20 °C).

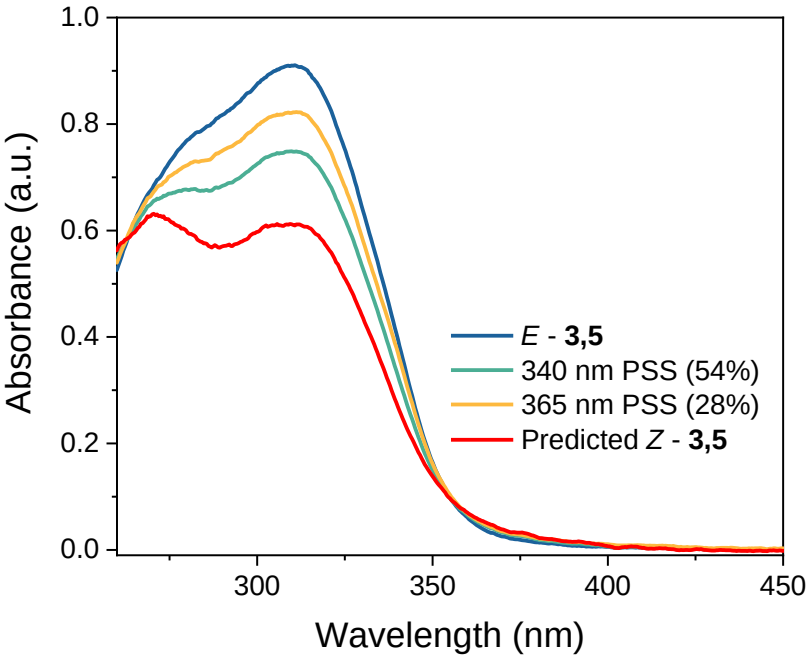

Figure S23. Absorbance spectra of the pure *E*-isomer and PSS at 340 and 365 nm and predicted absorbance spectra for the pure *Z*-isomer of IBP **3,5**. The measurements were carried out in MeCN (60 μM) at room temperature (20 °C).

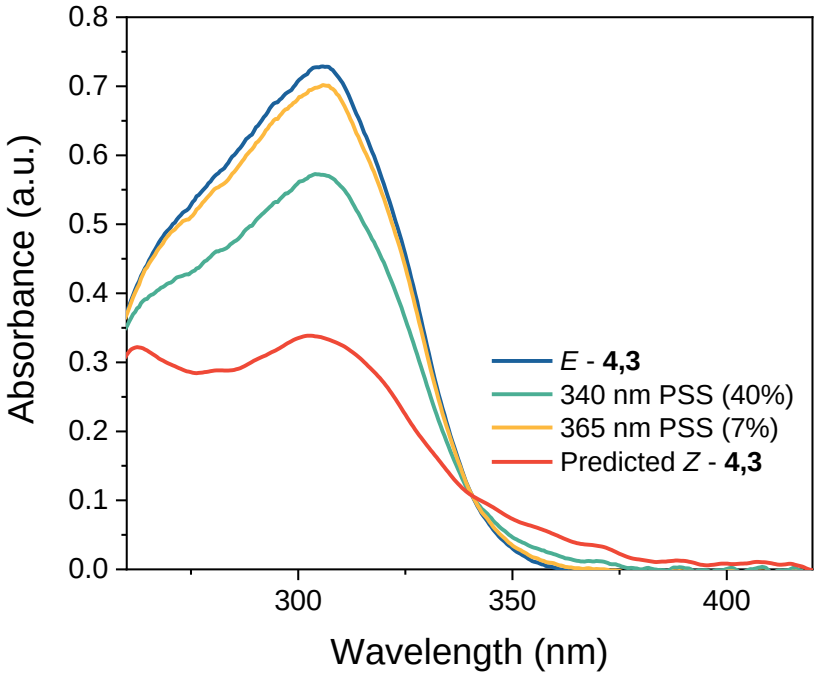

Figure S24. Absorbance spectra of the pure *E*-isomer and PSS at 340 and 365 nm and predicted absorbance spectra for the pure *Z*-isomer of IBP **4,3**. The measurements were carried out in MeCN (55 µM) at room temperature (20 °C).

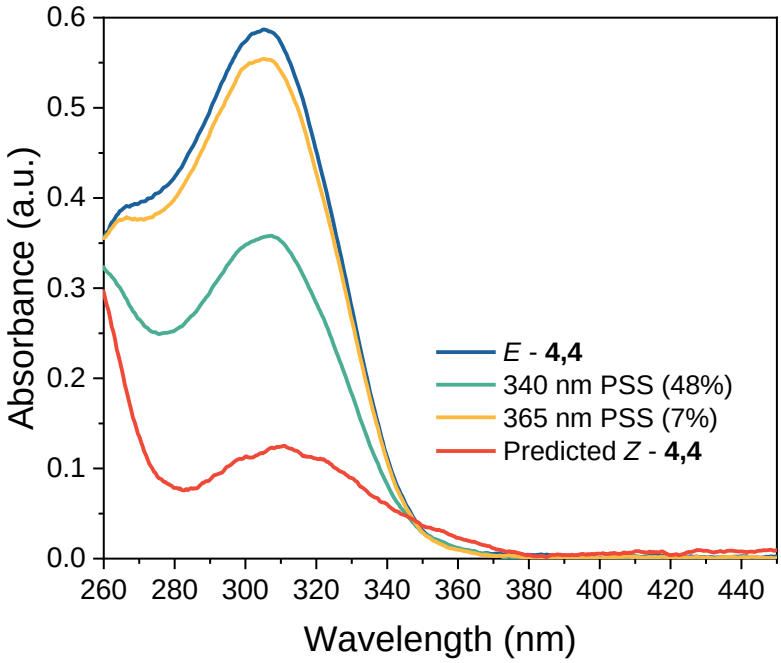

Figure S25. Absorbance spectra of the pure *E*-isomer and PSS at 340 and 365 nm and predicted absorbance spectra for the pure *Z*-isomer of IBP **4,4**. The measurements were carried out in MeCN (40 µM) at room temperature (20 °C).

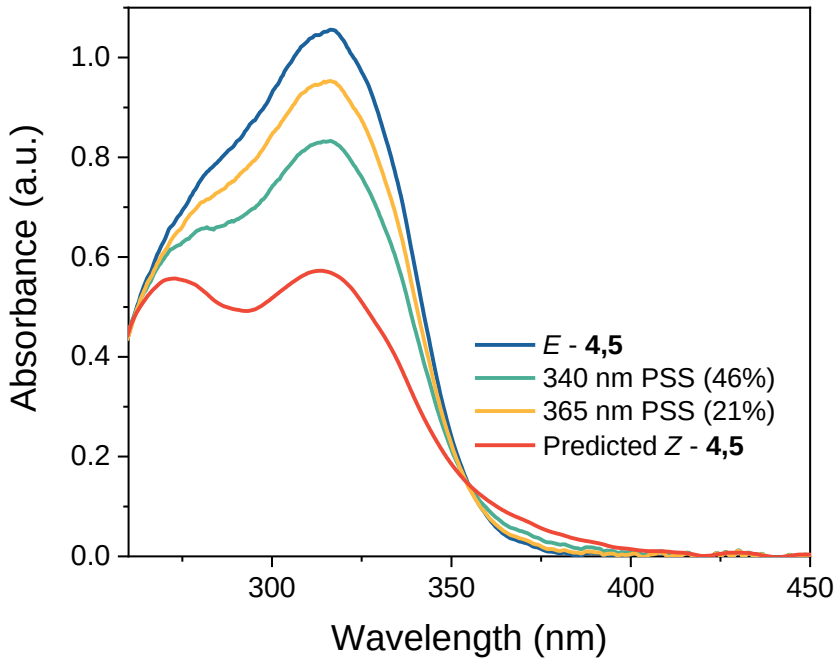

Figure S26. Absorbance spectra of the pure *E*-isomer and PSS at 340 and 365 nm and predicted absorbance spectra for the pure *Z*-isomer of IBP **4,5**. The measurements were carried out in MeCN (80 μM) at room temperature (20 °C).

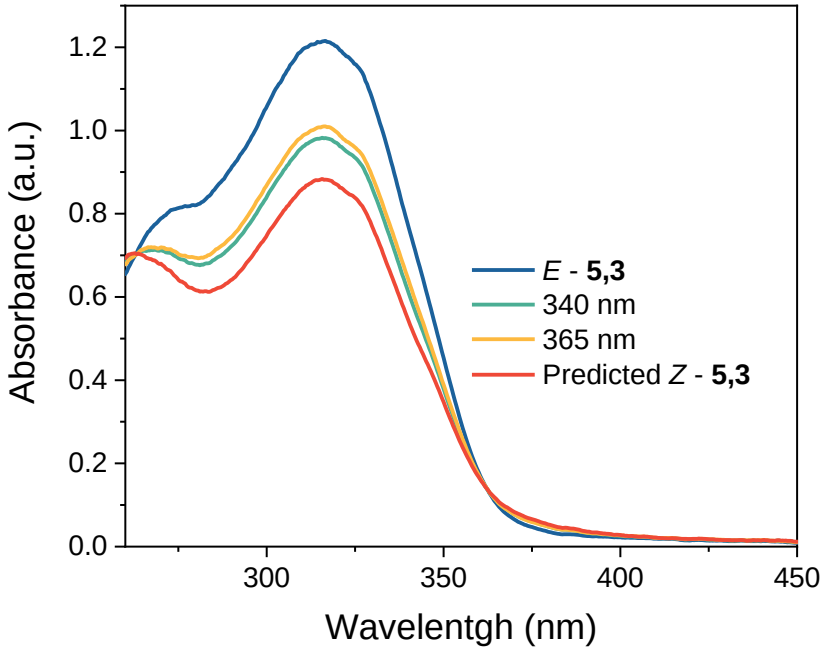

Figure S27. Absorbance spectra of the pure *E*-isomer and PSS at 340 and 365 nm and predicted absorbance spectra for the pure *Z*-isomer of IBP **5,3**. The measurements were carried out in MeCN (90 μM) at room temperature (20 °C).

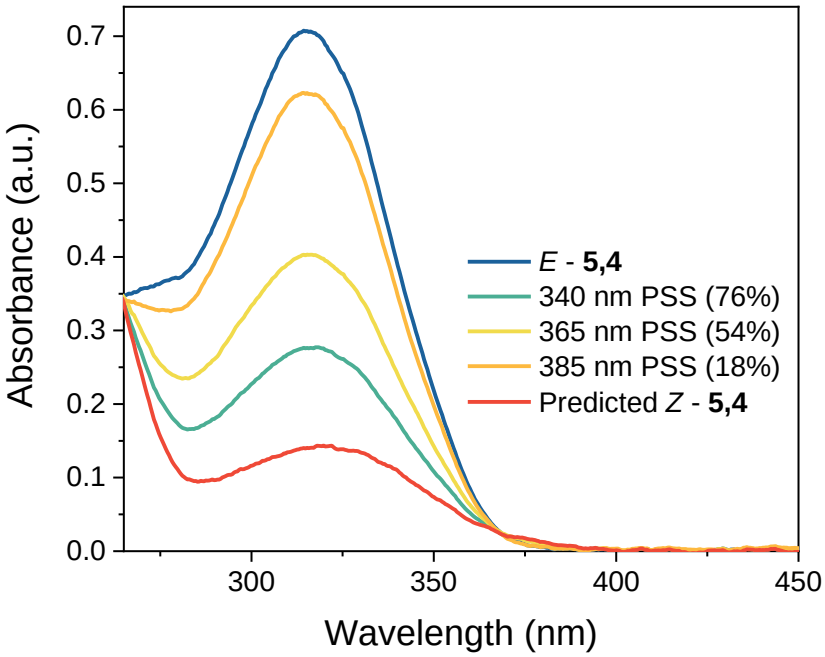

Figure S28. Absorbance spectra of the pure *E*-isomer and PSS at 340, 365, and 385 nm and predicted absorbance spectra for the pure *Z*-isomer of IBP **5,4**. The measurements were carried out in MeCN (50 μM) at room temperature (20 °C).

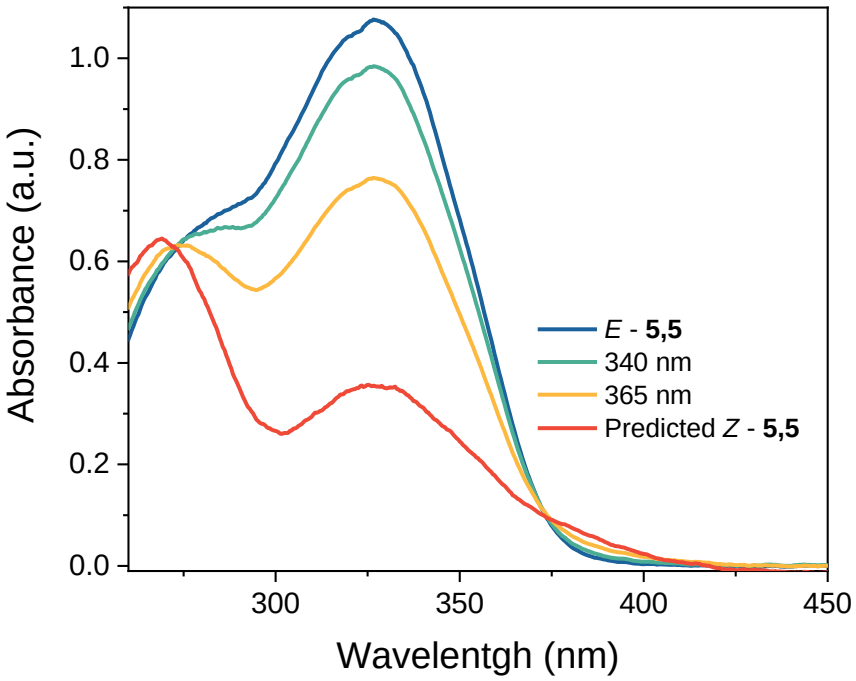

Figure S29. Absorbance spectra of the pure *E*-isomer and PSS at 340 and 365 nm and predicted absorbance spectra for the pure *Z*-isomer of IBP **5,5**. The measurements were carried out in MeCN (70 μM) at room temperature (20 °C).

4.4 Quantum Yield

The irradiation setup employed in this study was identical to that described in our previous work.[1] The photon fluxes provided by the light source with the wavelengths of 340 nm, 365 nm, 385 nm, and 405 nm are listed in Table S1. The quantum yield values of IBPs are listed in Table S3.

Table S5. The photon fluxes provided by light source with different wavelengths respectively.[1]

Wavelength	**Photon Flux** (Photons/s)
340 nm	4.25×10^{14}
365 nm	6.32×10^{14}
385 nm	7.38×10^{14}
405 nm	6.29×10^{14}

4.5 Fatigue Resistance

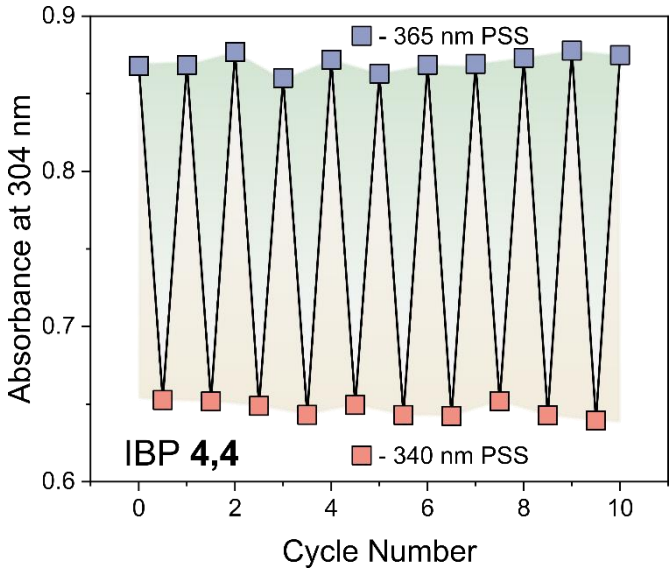

Figure S30. Plot showing the fatigue resistance of IBP **4,4** to repeated photoisomerism with 340 nm and 365 nm photoirradiation. No signs of degradation are observed over 10 switching cycles.

5. Computational Studies

All underlying (TD-)DFT calculations were performed using the ORCA 5.0.4 software.[7–9] Other programs we used as part of our approach are CREST 2.12[10,11] and CENSO 1.2.1[12] for conformational search, NCIPLOT 4.0[13–15] for intramolecular interaction analysis. Images of molecules were created with VMD 1.9.2[16] and Pymol.

Conformer Search and Geometry Optimisation of *E* and *Z* Isomers and Transition State

We investigated the thermally accessible conformers of the imine switches at room temperature using the Conformer-Rotamer Ensemble Sampling Tool (CREST). Based on metadynamics simulations[11] and stepwise optimisation at semiempirical GFN2-xTB level,[17–20] it is suitable for finding low-energy conformers quickly and efficiently. The identified conformers were then refined using the Commandline Energetic Sorting (CENSO) algorithm. This process ranked the conformers based on their free energy at DFT-level of theory and optimised their geometries further using the meta-generalized-gradient approximation (mGGA) functional r^{2}SCAN-3c in combination with a def2-mTZVPP basis set.[21] The geometries of the lowest energy *E* and *Z* conformers were further optimised at ωB97X-D4/def2-TZVPP level of theory with a CPCM solvation model for acetonitrile.[22–28] Ground-state equilibrium geometries of the *E* and *Z* isomers were confirmed by the absence of imaginary vibrational frequencies.

In previous studies,[1] we found that the E-Z isomerization of imines occurs via inversion of the C-N=C bond. Having identified these structures for all investigated imines, a conformational search of the transition state was applied using CREST. Therefore, the TS mode was fixed (α = 180°) and conformers were searched as described above. The lowest-energy conformers were subsequently optimized at ωB97X-D4/def2-TZVPP level and the resulting transition state with the lowest energy was selected for the following calculations. All transition states were confirmed by the presence of a single imaginary vibrational frequency.

Theoretical Investigation of Thermal Isomerisation Rates and Half-Lives

The rate of thermal isomerisation from the metastable *Z*-isomer to the thermodynamically stable *E*-isomer via the optimised transition state was be approximated using Eyring theory.[29] The rate, *k*, of *Z* to *E* isomerisation is given by equation (1),

$$k_{Z\to E}(T) = \frac{k_B T}{h} \cdot e^{\frac{-\Delta G^{\ddagger}}{RT}} \qquad (1)$$

where k_B is the Boltzmann constant, T is the temperature in Kelvin, h is the Planck constant, $\Delta G^{\ddagger}$ is the difference in the Gibbs energy of the *Z*-isomer and the transition state, and R is the gas constant. Once the rate is known, the thermal half-life, $t_{1/2}$, can be calculated from

$$t_{1/2} = \frac{ln\ 2}{k_{Z \to E}} \qquad (2)$$

Noncovalent Interaction (NCI) Analysis

Noncovalent interaction analysis was used to rationalize relationships between the geometries and thermal half-lives of the imine switches. This approach provides a visual representation of weak intramolecular interactions in the low-density regime. NCI analysis was performed using the NCIPLOT 4.0 program starting from the electron density of the optimized *E*, *Z* and TS structures obtained at ωB97X-D4/def2-TZVPP level.

Excited State Analysis

TD-DFT calculations were applied to investigate the photophysical properties of the imine switches. Here we used ωB97X-D4/def2-TZVPP to calculate the transition wavelengths and oscillator strengths. It is important to note that these long-range corrected functionals generally overestimate the excitation energies, which is why we shifted the broadened spectra by +50 nm to maximize agreement with the experimental spectra. We also performed Natural Transition Orbital (NTO)[30] analysis for the associated lowest energy singlet transitions in order to help assignment of the experimental UV/vis absorption bands.

Table S6. Summary of the theoretical data obtained for the IBPs.

IBP	$\Delta G^{\ddagger}$ (kJ mol^{-1})	$t_{1/2}$ (hh:mm:ss)	ΔG_{Z-E} (kJ mol^{-1})
3,3	86.97	00:06:02	16.49
3,4	89.99	00:20:54	13.93
3,5	81.06	00:00:32	17.99
4,3	78.28	00:00:10	26.84
4,4	93.61	01:32:14	11.29
4,5	83.90	00:01:42	20.14
5,3	83.25	00:01:18	15.76
5,4	86.30	00:04:35	10.06
5,5	64.14	00:00:00	30.33

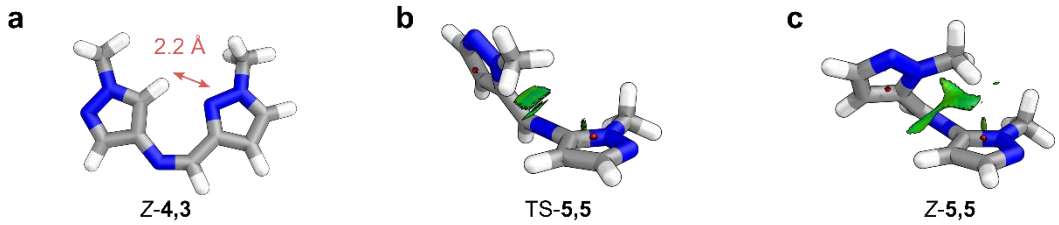

Figure S31. (a) The planar conformation of *Z*-**4,3** appears to be supported by an intramolecular hydrogen bond, this observation agrees with azo-based analogues reported by Li and co-workers.[31] It is interesting to note that *Z*-**3,4** does not adopt a planar geometry. (b) The transition state (TS) of **5,5** exhibits stabilizing non-covalent interactions (NCIs) between the methyl group of the pyrazole ring and the imine bond, contributing to a stabilization of the TS and thus a shortening of the $t_{1/2}$. (c) Extensive NCI surfaces are observed between the *N*−Me of the **−,5** unit and the *N*-pyrazole ring, contributing to a stabilization of the *Z*-isomer. This stabilization coming from the NCI interaction could be offset by the stabilization of the TS, shown in panel b.

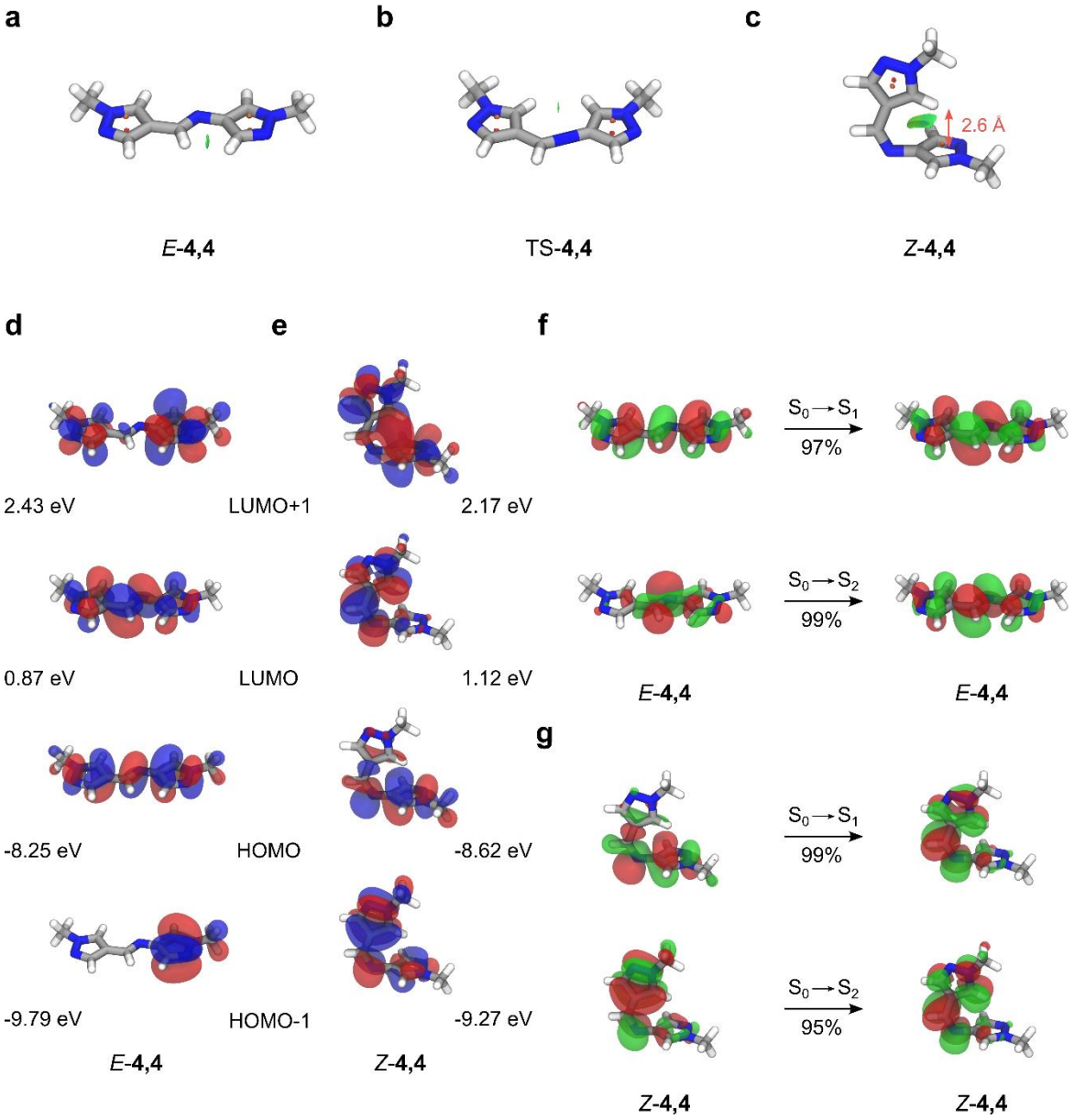

Figure S32. Overview of the theoretically calculated properties of the longest-lived IBP of the study, **4,4**. The geometry optimized structures, along with calculate non-covalent interaction (NCI) surfaces of (a) *E*-**4,4**, (b) TS-**4,4**, and (c) *Z*-**4,4** with the distance between the C−H of the pyrazole to the centroid of the *N*-pyrazole ring shown, indicating potential CH-π interactions. Frontier molecular orbitals (FMOs) of (d) *E*-**4,4** and (e) *Z*-**4,4** and corresponding energies. NTO pairs ("hole" → "particle") of the $S_0 \rightarrow S_1$ and $S_0 \rightarrow S_1$ transitions of (f) *E*-**4,4** and (g) *Z*-**4,4** with percentage contributions stated.

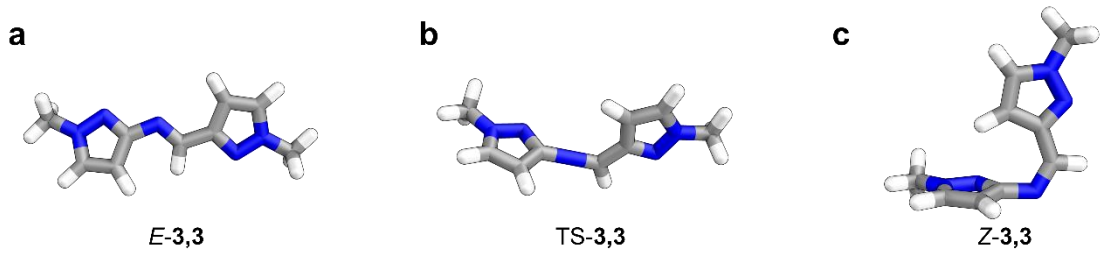

Figure S33. The geometry-optimized structures of IBP **3,3**. (a) *E*-**3,3**; (b) TS-**3,3**, indicating a preferred perpendicular geometry; (c) *Z*-**3,3**, showing a preference for a T-shape geometry.

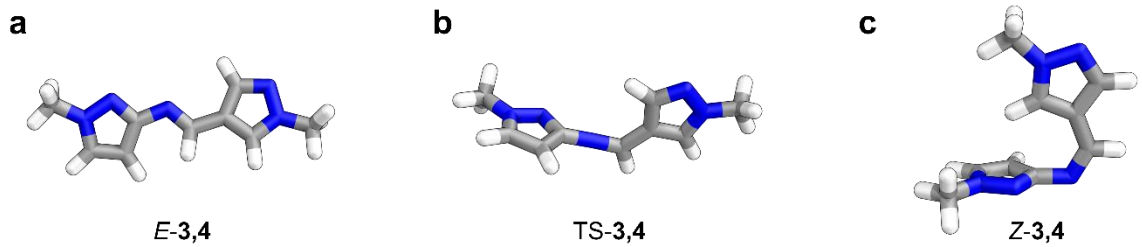

Figure S34. The geometry-optimized structures of IBP **3,4**. (a) *E*-**3,4**; (b) TS-**3,4**, indicating a preferred perpendicular geometry; (c) *Z*-**3,4**, showing a preference for a T-shape geometry. It is interesting to note that the *Z*-isomer for **3,4** adopts a different conformation from *Z*-**4,3** (Figure S36). We postulate that this is due to the relative electronics of the rings, indicating how the regiochemistry can cause a large impact on the preferred conformations.

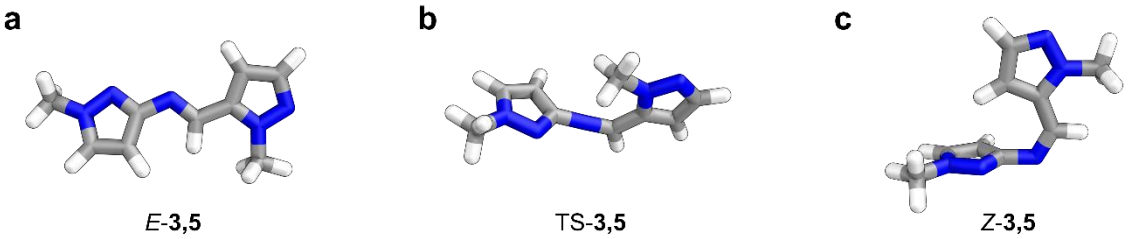

Figure S35. The geometry-optimized structures of IBP **3,5**. (a) *E*-**3,5**; (b) TS-**3,5**, indicating a preferred perpendicular geometry; (c) *Z*-**3,5**, showing a preference for a T-shape geometry.

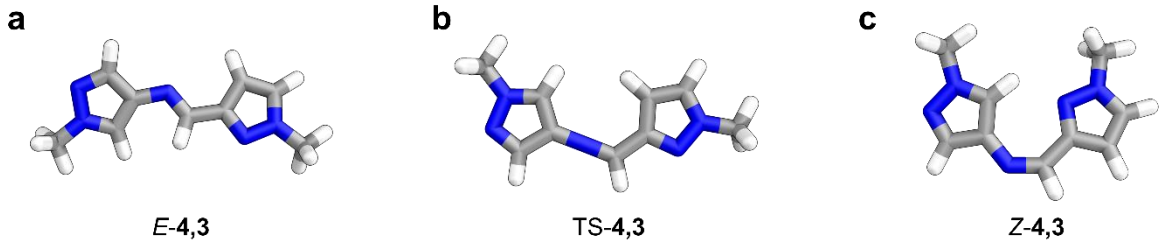

Figure S36. The geometry-optimized structures of IBP **4,3**. (a) *E*-**4,3**; (b) TS-**4,3**, indicating a preferred planar geometry; (c) *Z*-**4,3**, showing a preference for a planar geometry. This is consistent with the geometry found for the corresponding azobispyrazole switches reported by Li and co-workers.[31]

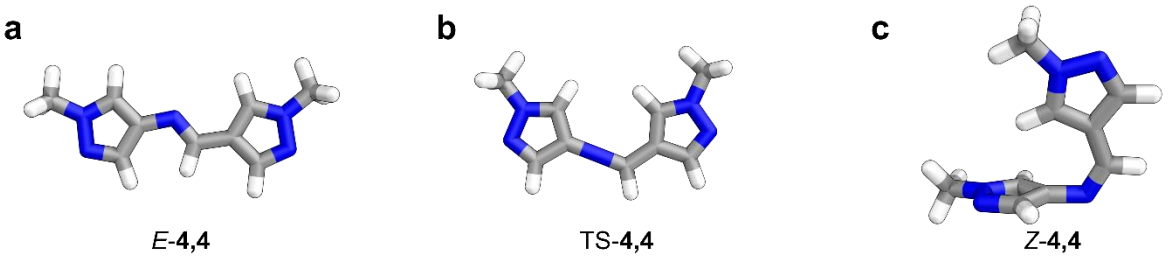

Figure S37. The geometry-optimized structures of IBP **4,5**. (a) *E*-**4,3**; (b) TS-**4,5**, indicating a preferred planar geometry; (c) *Z*-**4,5**, showing a preference for a T-shape geometry.

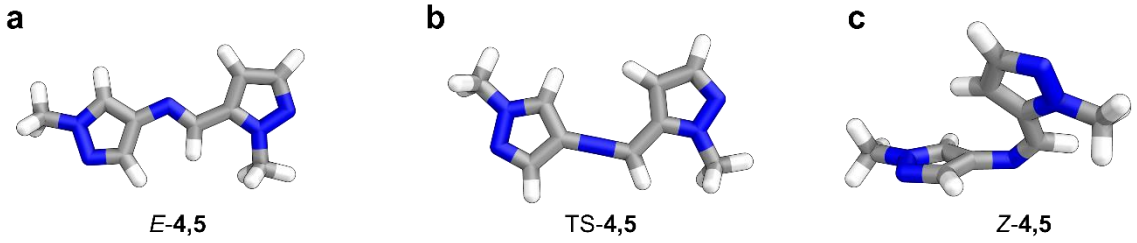

Figure S38. The geometry-optimized structures of IBP **4,5**. (a) *E*-**4,5**; (b) TS-**4,5**, indicating a preferred planar geometry; (c) *Z*-**4,5**, showing a preference for a twisted geometry.

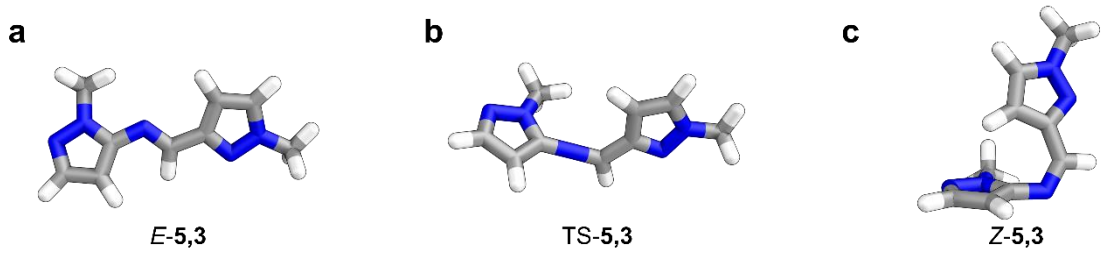

Figure S39. The geometry-optimized structures of IBP **5,3**. (a) *E*-**5,3**; (b) TS-**5,3**, indicating a preferred perpendicular geometry; (c) *Z*-**5,3**, showing a preference for a twisted T-shape geometry.

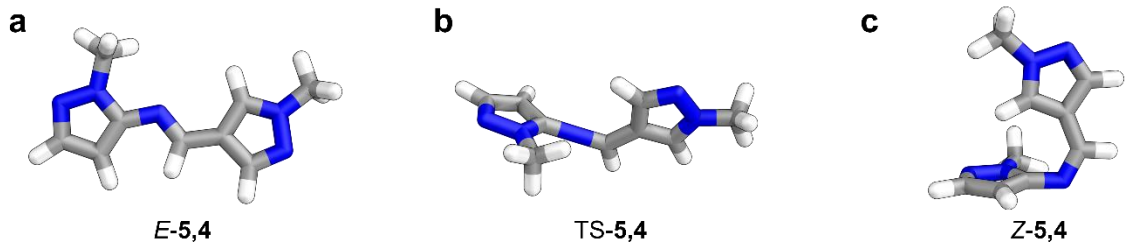

Figure S40. The geometry-optimized structures of IBP **5,4**. (a) *E*-**5,4**; (b) TS-**5,4**, indicating a preferred perpendicular geometry; (c) *Z*-**5,4**, showing a preference for a T-shape geometry.

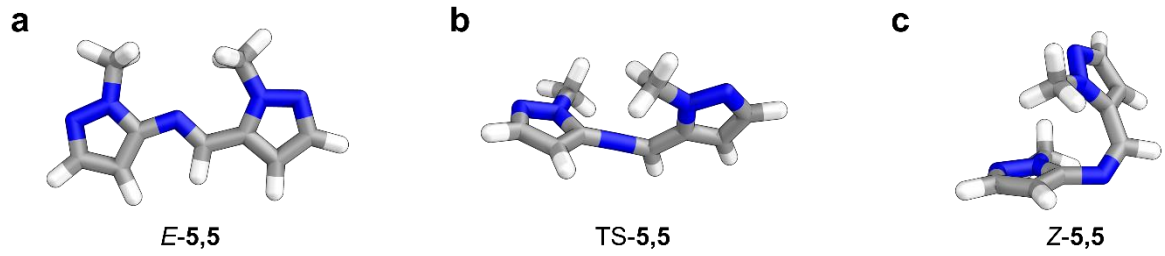

Figure S41. The geometry-optimized structures of IBP **5,5**. (a) *E*-**5,5**; (b) TS-**5,5**, indicating a preferred twisted perpendicular geometry; (c) *Z*-**5,5**, showing a preference for a twisted geometry.

References

1 J. Wu, L. Kreimendahl, S. Tao, O. Anhalt and J. L. Greenfield, *Chem. Sci.*, 2024, **15**, 3872–3878.

2 K. Stranius and K. Börjesson, *Sci. Rep.*, 2017, **7**, 41145.

3 G. M. Sheldrick, *Acta Crystallogr. A*, 2015, **71**, 3–8.

4 V. Gold, Ed., *The IUPAC Compendium of Chemical Terminology*, International Union of Pure and Applied Chemistry (IUPAC), Research Triangle Park, NC, 2019.

5 H. Eyring, *J. Chem. Phys.*, 1935, **3**, 107–115.

6 E. Fischer, *J. Phys. Chem.*, 1967, **71**, 3704–3706.

7 F. Neese, *WIREs Comput. Mol. Sci.*, 2012, **2**, 73–78.

8 F. Neese, *WIREs Comput. Mol. Sci.*, 2018, **8**, e1327.

9 F. Neese, F. Wennmohs, U. Becker and C. Riplinger, *J. Chem. Phys.*, 2020, **152**, 224108.

10 P. Pracht, F. Bohle and S. Grimme, *Phys. Chem. Chem. Phys.*, 2020, **22**, 7169–7192.

11 S. Grimme, *J. Chem. Theory Comput.*, 2019, **15**, 2847–2862.

12 S. Grimme, F. Bohle, A. Hansen, P. Pracht, S. Spicher and M. Stahn, *J. Phys. Chem. A*, 2021, **125**, 4039–4054.

13 E. R. Johnson, S. Keinan, P. Mori-Sánchez, J. Contreras-García, A. J. Cohen and W. Yang, *J. Am. Chem. Soc.*, 2010, **132**, 6498–6506.

14 J. Contreras-García, E. R. Johnson, S. Keinan, R. Chaudret, J.-P. Piquemal, D. N. Beratan and W. Yang, *J. Chem. Theory Comput.*, 2011, **7**, 625–632.

15 R. A. Boto, F. Peccati, R. Laplaza, C. Quan, A. Carbone, J.-P. Piquemal, Y. Maday and J. Contreras-García, *J. Chem. Theory Comput.*, 2020, **16**, 4150–4158.

16 W. Humphrey, A. Dalke and K. Schulten, *J. Mol. Graph.*, 1996, **14**, 33–38.

17 C. Bannwarth, E. Caldeweyher, S. Ehlert, A. Hansen, P. Pracht, J. Seibert, S. Spicher and S. Grimme, *WIREs Comput. Mol. Sci.*, 2021, **11**, e1493.

18 S. Grimme, C. Bannwarth and P. Shushkov, *J. Chem. Theory Comput.*, 2017, **13**, 1989–2009.

19 P. Pracht, E. Caldeweyher, S. Ehlert and S. Grimme, *ChemRxiv*, 2019, **29**, 8326202.

20 C. Bannwarth, S. Ehlert and S. Grimme, *J. Chem. Theory Comput.*, 2019, **15**, 1652–1671.

21 S. Grimme, A. Hansen, S. Ehlert and J.-M. Mewes, *J. Chem. Phys.*, 2021, **154**, 064103.

22 A. Najibi and L. Goerigk, *J. Comput. Chem.*, 2020, **41**, 2562–2572.

23 E. Caldeweyher, C. Bannwarth and S. Grimme, *J. Chem. Phys.*, 2017, **147**, 034112.

24 E. Caldeweyher, S. Ehlert, A. Hansen, H. Neugebauer, S. Spicher, C. Bannwarth and S. Grimme, *J. Chem. Phys.*, 2019, **150**, 154122.

25 E. Caldeweyher, J.-M. Mewes, S. Ehlert and S. Grimme, *Phys. Chem. Chem. Phys.*, 2020, **22**, 8499–8512.

26 F. Weigend and R. Ahlrichs, *Phys. Chem. Chem. Phys.*, 2005, **7**, 3297.

27 F. Weigend, *Phys. Chem. Chem. Phys.*, 2006, **8**, 1057.

28 V. Barone and M. Cossi, *J. Phys. Chem. A*, 1998, **102**, 1995–2001.

29 H. Eyring, *Chem. Rev.*, 1935, **17**, 65–77.

30 R. L. Martin, *J. Chem. Phys.*, 2003, **118**, 4775–4777.

31 Y. He, Z. Shangguan, Z. Zhang, M. Xie, C. Yu and T. Li, *Angew. Chem. Int. Ed.*, 2021, **60**, 16539–16546.

32 The relevant .xyz files of the geometry-optimized IBP molecules are available free of charge at DOI: 10.5281/zenodo.13383329